Cell Communication and Signaling

https://doi.org/10.1186/s12964-026-02693-7

Article in Press

Study of POLR3A variants in a family trio suggests mutation-specific pathogenetic mechanisms: insights from integrative OMIC approaches

Received: 13 October 2025

Accepted: 21 January 2026

Published online: 04 February 2026

Cite this article as: Rey F., Casamassa A., Cristofano S. *et al.* Study of POLR3A variants in a family trio suggests mutation-specific pathogenetic mechanisms: insights from integrative OMIC approaches. *Cell Commun Signal* (2026). https://doi.org/10.1186/s12964-026-02693-7

Federica Rey, Alessia Casamassa, Samuele Cristofano, Letizia Esposito, Amata Amy Soriano, Letizia Messa, Clarissa Berardo, Mahsa Hazrati, Ilaria Ferrone, Maxime Bonnet, Fabio Bruschi, Ylenia Vaia, Massimo Marano, Enrico Bertini, Francesco Nicita, Davide Tonduti, Gianvincenzo Zuccotti, Angelo Luigi Vescovi, Domenico Raimondo, Jessica Rosati, Stephana Carelli & Cristina Cereda

Study of POLR3A variants in a family trio suggests mutation-specific pathogenetic mechanisms: insights from integrative OMIC approaches

Federica Rey[1], Alessia Casamassa[2,+], Samuele Di Cristofano[3,+], Letizia Esposito[1,+], Amata Amy Soriano[2], Letizia Messa[4,5], Clarissa Berardo[1,4], Mahsa Hazrati[2], Ilaria Ferrone[2], Maxime Bonnet[1], Fabio Bruschi[6,7], Ylenia Vaia[6,7], Massimo Marano[8], Enrico Bertini[9], Francesco Nicita[9,10], Davide Tonduti[6,7], Gianvincenzo Zuccotti[1,11], Angelo Luigi Vescovi[12,13], Domenico Raimondo[3,*], Jessica Rosati[2,14,$,*], Stephana Carelli[1,4,*+,$], Cristina Cereda[1,4,*,+]

[1] Pediatric Clinical Research Center "Romeo ed Enrica Invernizzi", Department of Biomedical and Clinical Sciences, University of Milan, Milan, Italy

[2] Cellular Reprogramming Unit, Fondazione IRCCS Casa Sollievo della Sofferenza –Italy

[3] Department of Molecular Medicine, Sapienza University of Rome, Laboratory affiliated to Istituto Pasteur Italia – Fondazione Cenci Bolognetti, Rome, Italy

[4] Center of Functional Genomics and Rare Diseases, Department of Pediatrics, Buzzi Children's Hospital, Milan, Italy

[5] Department of Electronics, Information and Bioengineering, Politecnico di Milano, Milan, Italy.

[6] Unit of Pediatric Neurology, C.O.A.L.A (Center for Diagnosis and Treatment of Leukodystrophies), V. Buzzi Children's Hospital, Milan, Italy

[7] Department of Biomedical and Clinical Sciences, University of Milan, Milan, Italy

[8] Unit of Neurology, Neurophysiology and Neurobiology, Department of Medicine, Campus Bio-Medico of Rome University, Rome, Italy

[9] Research Unit of Muscular and Neurodegenerative Diseases, Bambino Gesù Ospedale Pediatrico, IRCCS, Rome, Italy

[10] Unit of Muscular and Neurodegenerative Diseases, Bambino Gesù Ospedale Pediatrico, IRCCS, Rome, Italy

[11] Department of Pediatrics, Buzzi Children's Hospital, Milan, Italy

[12] Faculty of Medicine, Link Campus University, Rome, Italy.

[13] Abu Dhabi Stem Cell Centre, Abu Dhabi, United Arab Emirates

[14] UniCamillus - Saint Camillus International University of Health Sciences, Rome, Italy.

[+] alphabetic order

[*] These authors contributed equally to the work

[$] Please address all correspondence to: Dr. Stephana Carelli, Center of Functional Genomics and Rare Diseases, Department of Pediatrics, Buzzi Children's Hospital, Milan, Italy. E-mail: stephana.carelli@asst-fbf-sacco.it. Tel. +39-02-50319825. Dr. Jessica Diana Rosati, Cellular Reprogramming Unit, Fondazione IRCCS Casa Sollievo della Sofferenza, San Giovanni Rotondo, Italy. E-mail: j.rosati@operapadrepio.it.

Abstract

Background: Hypomyelinating leukodystrophies (HLDs) are rare genetic neurodevelopmental disorders characterized by defective myelin formation. The genetic cause of these disorders has been ascribed to mutations in genes encoding myelin protein components, such as proteolipid protein 1 (*PLP1)* and myelin basic protein (*MBP)*, or in genes encoding for transcription and translation-related proteins. Particularly, biallelic pathogenic variants in *POLR3A*, *POLR3B*, *POLR3K*, *POLR3D*, *POLR1C* lead to the insurgence of RNA Polymerase III (Pol III)-related HLDs (POLR3-HLDs). The molecular mechanisms linking Pol III dysfunction to hypomyelination remain

largely elusive, though the main hypothesis is that impaired Pol III activity likely disrupts gene expression and cellular homeostasis processes critical for myelin development and lipid metabolism.

Methods: In this study, we analyzed a family trio consisting of unaffected carrier parents and a proband affected by *POLR3A*-related HLD, carrying compound heterozygous variants (p.Phe601Tyr and p.Gly1358Arg). We investigated the structural and functional consequences of two *POLR3A* variants using protein modeling, functional assays and multi-omics profiling in subject-specific primary fibroblasts.

Results: Structural analysis revealed alterations in DNA-binding regions and a likely impact on protein stability, whilst functional assays showed an impairment in cellular proliferation. Lipidomic and transcriptomic profiling revealed that p. Gly1358Arg mutation predominantly affects lipidomic metabolism, while p. Phe601Tyr was associated with a widespread transcriptional dysregulation. Both mutations ultimately caused a significant reduction in lipid droplets in the proband's cells.

Conclusions: These results demonstrate mutation-specific pathogenetic mechanisms in *POLR3A*-HLD and underline the utility of integrative multi-omics approaches in elucidating the molecular basis of rare neurodevelopmental disorders.

Key words

family trio, HLD, leukodystrophies, multi-omics approaches, POLR3, primary fibroblasts, RNA-Seq, transcriptional profile

1. Background

Leukodystrophies are a rare, genetically heterogeneous neurodevelopmental disorders with childhood onset, characterized by defective myelination of the central nervous system (CNS)(1). These conditions are broadly classified as either hypomyelinating or non-hypomyelinating, depending on whether the primary defect is a failure of myelin deposition during development or a disruption in myelin homeostasis and maintenance(2).

Hypomyelinating leukodystrophies (HLDs) typically present in early childhood or even during the neonatal period, with earlier onset generally correlating with more severe and progressive disease(3). Due to their substantial phenotypic variability, in terms of severity, age of onset and symptomatology, clear genotype-phenotype correlations are often lacking(4).

While some HLDs are directly caused by mutations in myelin genes (e.g. PLP, MBP), others result from mutations in genes involved in transcription and translation. In particular, biallelic pathogenic variants in *POLR3A*, *POLR3B*, *POLR3K*, *POLR1C* and *POLR3D*(5) cause RNA Polymerase III (Pol III)-related hypomyelinating leukodystrophies (*POLR3*-HLDs or HLD-7; OMIM: 607694) also known as 4H (hypomyelination, hypodontia, and hypogonadotropic hypogonadism) leukodystrophies(6–9). Moreover, a biallelic mutation in *POLR3GL* gene results in a disorder with similar clinical manifestations but without leukodystrophy(10).

Pol III is one of the three nuclear RNA polymerases, along with Pol I and Pol II, and it is responsible for transcribing a variety of small non-coding RNAs, including nuclear-encoded tRNAs (tRNA), 5S ribosomal RNA (rRNA), U6 small nuclear RNA (snRNA), 7SK RNA and several others that play critical roles in essential cellular processes, such as transcription regulation, RNA processing, and translation(11,12). Pol III is composed of 17 subunits, including a central ten-subunit catalytic core and a peripheral heterodimeric stalk, both structurally conserved across the three eukaryotic polymerases(13). *POLR3A* and *POLR3B* encode core catalytic subunits, whilst *POLR1C*, encodes a scaffold subunit shared with Pol I and Pol III, essential for complex assembly(14).

Although pathogenic variants in Pol III subunits are known to cause POLR3-HLDs, the molecular mechanisms linking transcriptional dysregulation to hypomyelination remain poorly understood. One prevailing hypothesis is that these mutations impair Pol III activity, altering the expression of critical non-coding and subsequently coding RNAs, thereby disrupting cellular homeostasis and developmental pathways required for myelination(15). Given that myelin is a lipid-rich structure composed predominantly of cholesterol, phospholipids (e.g., plasmalogen, phosphatidylcholine), glycolipids (e.g., galactosylceramide and its sulfated form, sulfatide) and sphingomyelin, precise regulation of lipid metabolism is essential(16). Indeed, myelination is a tightly regulated process requiring coordinated interaction among CNS cell types, including oligodendrocytes, astrocytes, microglia and neuronal axons(17).

Emerging evidence suggests that dysregulation of lipid metabolism may contribute to the pathogenesis of several leukodystrophies(18). Pathogenic mutations may affect the function of organelles involved in lipid metabolism and degradation, such as peroxisomes and lysosomes, ultimately leading to toxic lipid accumulation (as in GLA deficiency) or neuroinflammation (e.g. in ARSA deficiency)(18,19). However, the specific impact of *POLR3A* mutations on lipid metabolism and cellular function in HLD remains unknown.

Recently, integrative multi-omics studies have uncovered key mechanisms of human genetic disorders by combining functional genomics, transcriptomics and metabolomics. These approaches have proven instrumental in identifying novel disease-pathways and potential therapeutic targets(20–23).

Hence, in this study, we investigated an HLD-affected trio consisting of unaffected heterozygous carrier parents and an affected child harboring compound heterozygous *POLR3A* variants. This trio-based design allowed us to use each parent as a genetically matched control, enabling mutation-specific comparisons between the proband and each carrier parent. We identified a disease-associated cellular phenotype, which we further investigated using lipidomic and transcriptomic profiling of the trio to uncover mutation-specific molecular signatures. This integrative multi-omics

approach revealed deregulated pathways linked to lipid metabolism and transcriptional regulation, providing new insights into the mutation-specific molecular mechanisms that drive *POLR3*-HLD pathogenesis.

2. Methods

2.1 Isolation of fibroblasts from human skin biopsies

Skin punch biopsies (5mm diameter) were obtained from the volar forearms of one pediatric patient with *POLR3A*-HLD, her unaffected parents, and healthy controls matched for age and sex. Tissue fragments were cut into smaller fragments, plated overnight in 6 well plates with fetal bovine serum (FBS, Sigma-Aldrich) at 37°C and 5% CO_2 and then transferred in fibroblast medium composed by Dulbecco's Modified Eagle Medium (DMEM) High Glucose (Sigma-Aldrich) with 20% FBS (Sigma-Aldrich), 1% L-Glutamine (Sigma-Aldrich), 1% Penicillin-Streptomycin (Sigma-Aldrich) and 1% Non-Essential Amino Acids (Sigma-Aldrich). Fibroblasts migrating from tissue fragments were expanded until confluency. Before the collection of biological specimens, a signed informed consent form for tissue procurement previously approved by the Ethics Committee of the Institute "Casa Sollievo Della Sofferenza" was collected *(Casa Sollievo della Sofferenza Ethical Committee, approval number: 136/CE)*.

2.2 Sequencing

Genomic DNA was extracted from fibroblasts at passage VI using ReliaPrep™ Blood gDNA Miniprep System. *POLR3A* exon 14 was amplified by PCR using Forward: 5-GACTCTCAGGCTTCCTCCC-3, Reverse: 5-GGCACAGAGATCTTCCCCTT-3′ primers; *POLR3A* exon 31 was amplified by PCR using Forward: 5-TTCTGGTTGGTTTCAGGGGT-3, Reverse: 5-GGGGATGTGGAATTCATTTGTG-3′ primers. The amplicons (product size: 156 bp and 153 bp, respectively) were sequenced by BigDye terminator v.3.1 Cycle Sequencing kit on ABI 3130XL Genetic Analyzer.

2.3 Computational Methods

2.3.1 Model building

The cryo-EM structure of the elongating human RNA Polymerase III (POLR3A, UniProt ID: O14802) deposited in the Protein Data Bank with the best resolution (PDB ID: 7AE1) was selected as the starting model. Missing coordinates relative to the first two amino-terminal residues (M1, V2) were modeled using the RosettaRemodel application(24). Missing residues corresponding to the flexible linker (res. 266-275, UniProt numbering) were built using Rosetta Next-Generation Kinematic (NGK) loop modelling algorithms(25), to generate a total of 50 models. The best-scoring model was selected for downstream analysis.

2.3.2 Predicted changes in folding free energy

Rosetta ΔΔG calculations

Stability calculations for the three point-mutations were performed using the application cartesian-ddg(26,27) in the Rosetta software suite. First, the structures were minimized in cartesian coordinates using the relax application, the ref2015_cart score function, and constraints to starting coordinates. The relax protocol was run 20 times and the lowest scoring structure was chosen. The prepared starting structures were then run through the cartesian-ddg protocol, which scores each mutation in Rosetta Energy Unit (R.E.U.) by: 1) Selecting the lowest-energy score rotamer for the mutated residue. 2) Running five independent minimizations, during which only side-chain atoms within 6 Å of the mutation and backbone atoms in the mutated residue ±1 neighbor may move. 3) Averaging the R.E.U. scores from those five minimized models. ΔΔG scores are computed by performing the same protocol at each site while choosing the best wild-type (wt) rotamer at the first step, and then taking the difference between the mutant and WT energies. Finally, the ΔΔG values were scaled down to fit the overall scale of estimated values to actual experimental free energies measured in kcal/mol, using a scaling factor of 0.294.

The clini used to define the mutation classes is a $\Delta\Delta G < -1$ kcal/mol for stabilizing mutations, $-1 < \Delta\Delta G < 1$ kcal/mol for neutral mutations and $\Delta\Delta G > 1$ kcal/mol for destabilizing mutations (26,27).

The full set of command line flags for the relax and cartesian-ddg protocols are shown below:

relax flags:

<path/to/Rosetta>/main/source/bin/relax.default.linuxgccrelease \

-s <path/to/pdb_file> \

-out:path:all <path/to/output_dir> \

-database <path/to/Rosetta>/main/database \

-use_input_sc \

-constrain_relax_to_start_coords \

-ignore_unrecognized_res \

-nstruct 20 \

-relax:cartesian \

-relax:coord_constrain_sidechains \

-relax:min_type lbfgs_armijo_nonmonotone \

-score:weights ref2015_cart \

-relax:script cart2.

cart2.script:

switch:cartesian

repeat 2

ramp_repack_min 0.02 0.01 1.0 50

ramp_repack_min 0.250 0.01 0.5 50

ramp_repack_min 0.550 0.01 0.0 100

ramp_repack_min 1 0.00001 0.0 200

accept_to_best

endrepeat

cartesian-ddg flags*:*

<path/to/Rosetta>/main/source/bin/cartesian_ddg.linuxgccrelease \

-database <path/to/Rosetta>/main/database \

-s <path/to/relaxed_pdb_file> \

```
-out:path:all <path/to/output_dir> \
-ddg:mut_file <path/to/mut_file> \
-ddg:output_dir <path/to/output_dir> \
-ddg:iterations 5 \
-ddg::cartesian \
-ddg::dump_pdbs true \
-ddg::bbnbrs 1 \
-fa_max_dis 9.0 \
-score:weights ref2015_cart
```

Example *mut_file*, which specifies the mutation to make (here, F601Y). One such *mut_file* is used for each modeled mutation.

```
total 1    # specifies only one mutation is being made
1          # specifies only one mutation is being made
F 601 Y # mutation
```


FoldX calculations

We used FoldX 5.0(28,29) to predict the effect of point-mutations on protein stability through the approximation of Gibbs free energy (ΔG), relying on an empirical force field that is trained directly on experimental data. The FoldX *Repair PDB* function was used to optimize the wt PDB file and optimize side-chain orientations for mutant stability calculation. Next, for each mutation, we obtained the mutant structure based on the optimized wt structure of *POLR3A*. The resulting coordinates were then processed to calculate the change in folding free energy of the mutants relative to the wt protein ($\Delta\Delta G_{MUT} = \Delta G_{MUT} - \Delta G_{WT}$). A positive $\Delta\Delta G_{MUT}$ ($\Delta\Delta G_{MUT} > 0$ kcal/mol) suggests that the mutant protein is less stable than the wt protein.

DynaMut2 calculations

The optimized wt structure obtained with Rosetta, alongside the respective mutant residues at their corresponding positions, were also used as input for the Dynamut2's algorithm(30). DynaMut2 integrates normal mode analysis with statistical potentials to predict the structural and functional consequences of point mutation(30). Predictions were derived from changes in folding free energy (ΔΔG), providing insights into how genetic variants may perturb protein conformation and stability. A positive $\Delta\Delta G_{MUT}$ ($\Delta\Delta G_{MUT} > 0$ kcal/mol) suggests that the mutant protein is less stable than the wt protein.

Predicted pathogenicity and associated molecular mechanism

MutPred2

To assess the pathogenic potential of amino acid substitutions, we employed MutPred2(31), MutPred2 is a neural-network–based tool for evaluating how likely an amino acid change is to cause disease. Trained on over 250,000 curated variants from sources like HGMD, Swiss-Prot and dbSNP, it outputs: i) a global pathogenicity score – the probability that the variant is disease-causing: ii) predicted molecular mechanisms – which structural or functional protein features the variant may disrupt. iii) property scores (Pr) and p-values – statistical measures supporting each predicted mechanism. iv) impacted sequence motifs – any PROSITE or ELM motifs altered by the substitution.

General scores vary from 0.0 (benign) to 1.0 (pathogenic), where with $g \geq 0.5$ would suggest pathogenicity; The Pr score is the posterior probability of loss or gain (whichever is greater) of the given property due to the substitution. The higher the Pr score, the more likely that the molecular mechanism of the disease involves the alteration of the property.

AlphaMissense

We employed the AlphaMissense framework integrated in the AlphaFold Protein Structure Database (AlphaFold DB)(32) (https://alphafold.ebi.ac.uk/entry/O14802) to evaluate the pathogenic potential of amino acid substitutions. Based on AlphaMissense scores (AM score), variants were classified as likely benign (0.000 - 0.340), uncertain (0.350 - 0.564), or likely pathogenic (0.564 -

1.000). AM score is computed on integrative features, including predicted structural context, evolutionary conservation, and protein language modeling. Pathogenicity was quantified as the log-likelihood difference relative to the wt residue(33).

SIFT

SIFT (Sorting Intolerant From Tolerant) is a sequence homology–based method used to estimate the likelihood that a missense variant will adversely affect protein function. It calculates the normalized probability of observing a specific amino acid substitution at a given position; scores ranging from 0 to 0.05 are predicted to affect protein function and are therefore classified as deleterious(34).

PolyPhen-2

PolyPhen-2 integrates both sequence- and structure-based features to evaluate the potential impact of amino acid substitutions, taking into account the evolutionary distance from the earliest diverging homolog. Although PolyPhen-2 uses the same scoring range as SIFT (0.0 to 1.0), the interpretation is opposite: variants with scores closer to 1.0 are predicted to be deleterious(35).

MutationTaster

MutationTaster predicts the effects of missense mutations across all protein-coding Ensembl transcripts and aligns homologous isoforms from ten additional species for conservation analysis. It classifies substitutions as either “deleterious” or “benign.” In this study, we used MutationTaster 2025, which is based on the current human genome assembly, GRCh38(36).

AFFIPred

AFFIPred is an ensemble machine learning model that integrates both sequence-based features and AlphaFold2-derived structural features, including pLDDT scores and solvent-accessible surface area. AFFIPred produces scores ranging from 0.0 to 1.0, with higher

values indicating a greater likelihood of pathogenicity. In addition, a confidence ranking system based on the mean score and standard deviation is provided(37).

StructMAn 2.0

StructMAn 2.0 characterizes each variant position based on its structural relevance within the three-dimensional protein framework and its involvement in protein–protein interactions. The StructMAn 2.0 workflow consists of four main steps: (1) structure search, (2) sequence alignment, (3) structural analysis, and (4) data aggregation. Based on these structural indicators, we inferred the potential impact of our missense variants(38).

Meta-EA$_{clinical}$

The Meta-EAclinical classifier integrates Meta-EA scores with predicted splicing effects and allele frequency data of human polymorphisms, enabling a more refined clinical assessment of single amino acid substitutions. The scoring system provides a percentage value representing the probability that a substitution is “more neutral” (0%) or “more deleterious” (100%)(39).

2.4 Western Blot analysis

Cells were washed twice with ice-cold PBS and lysed in 1X RIPA buffer (Cell Signaling) containing phosphatase and protease inhibitors (Sigma-Aldrich). Protein concentration was measured using the BCA assay (Bio-Rad). Lysates were run on 4–15% Mini-PROTEAN TGX gels (Bio-Rad) and transferred to PVDF membranes using the Trans-Blot Turbo system. Membranes were washed in TBS with 1% Tween-20 (TBS-T) (Thermo Fisher), then blocked with 5% non-fat milk in TBS-T for 1 hour at room temperature. Primary antibodies (anti-POLR3A 1:500 – Abcam, anti-GAPDH 1:1000 – Sigma-Aldrich) were applied overnight at 4°C. After three washes in TBS-T, membranes were incubated with HRP-conjugated secondary antibodies (anti-mouse 1:3000, anti-rabbit 1:5000 – GE Healthcare) for 1 hour at room temperature. Detection was performed using ECL Prime (GE Healthcare), and signals were acquired with the ChemiDoc XRS+ system (Bio-Rad). Image analysis and densitometry were carried out using ImageJ.

2.5 Cell Culture and Growth Curves

Fibroblasts were cultured in DMEM High Glucose supplemented with 20% FBS (Sigma-Aldrich), 2mM L-Glutamine (Sigma-Aldrich), 100U/mL Penicillin-Streptomycin (Sigma-Aldrich) and 1x Non-essential Amino Acids (Sigma-Aldrich) at 37°C, 5% CO_2. For all experimental procedures, cells were seeded and treated the next day with 1 µM dexamethasone for 2 h to induce circadian synchronization, followed by media replacement. After 22 h, cells were collected for analysis. Growth and cell death (% Trypan Blue-positive cells) were assessed at days 7, 14, and 21. Oleic acid (50 µM, Sigma-Aldrich) was added throughout the experiment in treated conditions only. Growth was reported as the ratio of counted to plated cells; mortality was calculated as the % of trypan blue- stained cells. All experiments were done in triplicate unless stated otherwise.

2.6 Oil Red O staining and oleic acid supplementation

To assess lipid accumulation, ~5,000 fibroblasts/well were plated in 96-well plates, synchronized with 1 µM dexamethasone for 2 h, and treated with 50 µM oleic acid or vehicle for 24 h. Cells were fixed in 4% paraformaldehyde (PFA) for 30 min, and stained with Oil Red (O1257-Sigma-Aldrich) for 45 minutes. Specifically, the working solution (stock in 100% 2-propanol, diluted 2:3 with H_2O and filtered) was prepared per manufacturer's instructions. Cells were then washed and counterstained with Hoechst 33342 (Thermo Fisher Scientific, 1:10,000, 5 min). Imaging was performed on a Nikon C2 microscope (40×). Lipid droplets and nuclei were quantified using ImageJ across 10 fields per condition, and results are expressed as average LDs per cell.

2.7 RNA Extraction and Library Preparation

Total RNA from fibroblast cells was extracted using TRIZOL® reagent (Thermo Fisher Scientific) following manufacturer's instructions, quantified on a Multiskan GO spectrophotometer, and

quality-assessed using the TapeStation 4200 (Agilent). Three cellular replicates per patients were processed. Ribosomal RNA was removed using the RiboCop kit (Lexogen), and RNA-seq libraries were prepared with the CORALL Total RNA-Seq Library Prep Kit (Lexogen) using 500 ng total RNA. The quality and quantity of the prepared libraries was assessed with D1000 ScreenTape Assay using the 4200 TapeStation System (Agilent). Libraries were sequenced using 75 bp paired-end reads on the Illumina NextSeq 500 platform (Illumina).

2.8 RNA-Seq bioinformatics data analysis

Reads were demultiplexed with Illumina bcl2fastq2 (v. 2.17.1.14). The quality of the raw data output was examined with FastQC. Because CORALL libraries contain N12 UMIs at the start of Read 1, UMIs were removed in the first step using the UMI tools software. Adapter sequences, poly(A) sequences at the 3′ end of Read 1, and poly(T) sequences at the 5′ end of Read 2 were then trimmed using the Cutadapt software. Subsequent steps to assess gene and transcript intensities were carried out using the STAR software and transcripts were aligned on the GRCh38 version of the genome. Gene and transcript abundance were computed using the FeatureCounts software (stranded forward).

Differential gene expression analysis was carried out using the R package DESeq.2; coding and non-coding genes were considered differentially expressed and retained for further analysis when $|\log_2 FC| \geq 1$ and FDR ≤ 0.1.

The R software was used to generate PCA plots (the prcomp function from the R ggplots package), whilst over-representation analysis (ORA) for Wikipathways and KEGG were carried out using ClusterProfiler(40). A Venn diagram for shared genes was constructed using the InteractiVenn webtool(41).

2.9 Lipidomics Analysis

For lipidomic analysis, $1*10^6$ cells were plated in a 6-well plate. 3 cell pellets per patient were then collected in PBS and samples were analyzed at Unitech OMICS (University of Milan, Italy), a facility for proteomic, lipidomic and metabolomic studies based on mass spectrometry. Data

analysis was performed with the MS-DIAL program integrated with the LipidBlast database. The lipidomic differentially expressed data was defined as lipids with an abundance ration >2 or <0.5. Lipid Enrichment analysis was performed with the LION/web tool(42) to obtain Heatmaps of lipid amounts. A PCA plot was constructed using the prcomp function from the R ggplots package. A Venn diagram for shared lipids was constructed using the InteractiVenn webtool(41). BioPAN webtool was used for the analysis of activated and suppressed pathways from dysregulated lipids(43). The MetaboAnalyst 5.0 webtool was used to cross-reference and perform combined enrichment analysis for lipidomic and transcriptomic analysis(44,45).

2.10 Quantitative Real-Time PCR analysis (qPCR)

1000 ng of RNA were retro transcribed using the Supermix 5X (Genespin) enzyme following manufacturer's instructions. qPCR was performed using the CFX Connect Real-Time PCR System (Bio-Rad) using Optimum qPCRMaster Mix with SYBR® Green (Genespin). The NCBI's Primer-BLAST tool was used to design primers. *POLR3A* mRNA expression analysis was carried out with 7900HT Fast Real-Time PCR system (Applied Biosystem) using Power SYBR Green PCR Master Mix (Applied Biosystem). Each sample was tested in technical triplicate across three cellular replicates.

Gene expression was quantified using the $2^{-\Delta\Delta Ct}$ method. TBP was used as endogenous control for all genes except *POLR3A*, for which β-ACTIN was considered as the reference gene. The list of primers used is reported in Table 1.

Table 1. List of primers used in this work.

Gene	Forward	Reverse
SCD1	TGCAGGACGATATCTCTAGC	ACGATGAGCTCCTGCTGTTA
PTDSS1	GAAAGGGACAAAAGGTTCTG	TTGGTGACTTTTGACTTGGA
ELOVL5	CCTTGGGCTAAAAGGTTTTCAA	GTATCTCGAGGGCCTAGCAA
TBP	TTAACTTCGCTTCCGCTGGC	CAAGAAACAGTGATGCTGGGTCA
POLR3A	ATGGGGAACCGCTGATTGCT	TCCACAGGGTGACAGGCTTTA

β-ACTIN	GGCATCCTCACCCTGAAGTA	GGGGTGTTGAAGGTCTCAAA

2.11 Statistical Analysis

Differences in variables among patients were evaluated through t-test, One-way ANOVA and Two-way ANOVA followed by Sidak test for multiple comparison, when required. Statistical analyses were performed using GraphPad Prism software version 8.0. Results are presented as means ± SD or ± SEM. p values ≤ 0.05 were considered statistically significant. *p ≤ 0.05, **p ≤ 0.01, ***p ≤ 0.001, **** p ≤ 0.0001 compared as indicated in the graphs.

3. Results

3.1 Clinical characteristics of the proband

The proband is a 12-year-old girl, the second child of non-consanguineous healthy Italian parents. Her older brother had previously been diagnosed with *POLR3A*-HLD, he had a history of congenital nystagmus and psychomotor delay, never acquired autonomous walking and died at age 12 years due to septic shock after pneumonia (Figure 1A). Both parents are clinically healthy, with no neurological or systemic signs ascribable to hypomyelinating leukodystrophy or related disorders. No subclinical abnormalities were reported during clinical evaluation or follow-up.

The proband was born at 34 weeks of gestational age by cesarean section due to threatened preterm labor, and no hypoxic-ischemic insult occurred at birth. Birthweight was 2420 gr and birth length was 50 cm. Neonatal period was normal. Cognitive and motor milestones were normally acquired in the first two years of age: she pronounced first words by age 12 months and acquired autonomous walking by age 14 months. At age 2, she manifested horizontal nystagmus though the first neurological examination was reported as normal. By age 5, following a respiratory infection, the patient manifested cognitive and motor regression with development of dysarthria and ataxia and loss of autonomous walking. Myopia was noticed at age 7. Neurodegeneration progressed over time with the development of slowly progressive appendicular spasticity and foot dystonia, development of anarthria by age 9, loss of head control by age 10, and appearance of dysphagia with recurrent

lower respiratory tract infections. Percutaneous endoscopic gastrostomy was placed at age 11 and half and exclusive enteral nutrition was started. At age 11, evoked potentials (i.e., visual, brainstem and somatosensory) showed alteration of both optic pathways, upper pons and somatosensory tracts, and brain magnetic resonance imaging confirmed the presence of diffuse hypomyelination of the cerebral and cerebellar white matter, thin corpus callosum and mild cerebellar atrophy. Last neurological examination at age 11 years and half showed anarthria but conserved eye contact and ability to follow objects in a horizontal plane with vertical gaze palsy, subcontinuous pendular nystagmus, apostural spastic-dystonic tetraparesis. She is under therapy with clonazepam and gabapentin.

Genetic analysis identified a compound heterozygous genotype in POLR3A, with one variant inherited from each parent (c.1802T>A, p.Phe601Tyr)(46). The first variant (c.1802T>A) is a VUS inherited from the mother while the second ones is a variant inherited from the father (c.4072G>A).

3.2 Collection of trio primary fibroblasts and *POLR3A* variations analyses

This study included six primary fibroblast lines obtained from skin biopsies (Table 2): three from the affected family trio (Proband – HLD7, unaffected mother – carrier mother, unaffected father – carrier father) and three from age- and sex-matched healthy donors, used as controls (pediatric control – CTR HLD7, female control – CTR mother, male control – CTR father).

Table 2. List of samples used in this study.

Patient's ID code	**Age at biopsy (y.o.)**	**Gender**	**Mutated Gene**	**Mutated Sequence**
HLD7	10	Female	*POLR3A*	NM_007055: c.1802T>A, p.Phe601Tyr; c.4072G>A, p.Gly1358Arg
CARRIER MOTHER	53	Female	*POLR3A*	NM_007055: c.1802T>A, p.Phe601Tyr
CARRIER FATHER	58	Male	*POLR3A*	NM_007055: c.4072G>A, p.Gly1358Arg
CTR HLD7	10	Female	N/A	N/A

CTR MOTHER	56	Female	N/A	N/A
CTR FATHER	55	Male	N/A	N/A

After cell lines establishment, Sanger sequencing was performed to verify the presence and inheritance of *POLR3A* variants. As expected, each parental primary fibroblast line carried a single heterozygous mutation, while the proband was compound heterozygous for both variants (Figure 1B). Specifically, the paternally inherited c.4072G>A mutation is localized on exon 31 while the maternal c.1802T>A mutation lies within exon 14(Figure 1C). Mapping of both missense variants onto the three-dimensional structure of PolIII revealed their localization in distinct functional domains, as illustrated using a color-coded domain scheme (Figures 1C-1D). To assess the structural impact of the variants consequences, we calculated changes in protein stability (ΔΔG) using Rosetta, FoldX, and DynaMut 2.0. Both p.Phe601Tyr (F601Y) and p.Gly1358Arg (G1358R) exhibited positive ΔΔG values across all methods, indicating a destabilizing effect on the protein folding (Figure 1E). Consistently, AlphaMissense assigned high pathogenicity scores to both variants (0.95 for F601Y and 0.98 for G1358R), supporting their deleterious nature (Figure 1D). Structural analysis revealed that F601Y disrupts conserved hydrophobic interactions within the buried pore 1 region by introducing a hydroxyl group, while G1358R introduces new local contacts, including potential cation–π interactions, which may reduce flexibility and alter clamp architecture (Figure 1F). To explore potential mechanistic consequences of these variants, we utilized MutPred2, a machine learning-based method that predicts molecular alterations associated with missense mutations (Figure 1G). MutPred2 predicted altered DNA binding for F601Y — compatible with its location in the nucleotide entry path — and disruption of ordered subunit interfaces for G1358R, potentially interfering with the overall assembly or function of the RNA Polymerase III complex (Figures 1F, G).

We further assessed variant pathogenicity using multiple amino acid substitution prediction tools. The SIFT analysis led up to the characterization of both F601Y and G1358R as “tolerated” missense mutations, respectively with scores of 0.08 and 0.06. In contrast, both PolyPhen-2 and MutationTaster supported the pathogenic potential of the two substitutions. In PolyPhen-2, F601Y was defined as “possibly damaging”, with a score of 0.954, while G1358R was classified as “probably damaging”, with a score of 1.000. In MutationTaster, both mutations were classified as “deleterious”. The AFFIPred server further confirmed these findings, ranking both F601Y and G1358R as “pathogenic”, although with different confidence levels: F601Y only received a one star rating, with an average score of 0.59 ± 0.1, while G1358R achieved a three star rating, with a score of 0.89 ± 0.02. Structural role analysis using StructMAn 2.0 software, which described the structural roles of individual residues, indicated that Phe601 is a critical component of the POLR3A core, supporting the conclusion that the F601Y substitution may destabilize the overall protein structure. In contrast, G1358R was found to be important not only for core stability but also for interaction with the POLR3B subunit; therefore, the G1358R mutation may lead to the loss of this interaction. Finally, to further evaluate the predicted clinical impact of the variants of interest, we performed a Meta-$EA_{clinical}$ assessment. F601Y received a score of 23.08%, suggesting a moderate deleterious effect, whereas G1358R reached a score of 63.52%, indicating a substantially more deleterious clinical impact.

3.3 Cellular phenotypes in primary fibroblasts from the *POLR3A-HLD trio*.

To investigate the functional impact of POLR3A variants at the cellular level, we first assessed *POLR3A* mRNA expression across the trio and matched healthy controls. No significant differences were observed in POLR3A transcript levels either between the trio versus controls (Figure 2A) or among trio members (Figure 2B). At the protein level, *POLR3A* expression was comparable between the proband (HLD7) and the mother (Carrier Mother) compared to healthy control cells. Instead, a significant increase was present in father’s cells with respect to sex and age matched

control (Figure 2C). Intra-trio comparisons confirmed that both the proband and the mother had significantly lower POLR3A protein levels compared to the father (Figure 2D).

Next, we evaluated the effects of POLR3A variants on cellular proliferation. A significant reduction in proliferation was observed in all trio members when compared to their respective matched controls (Figure 2E), whereas an increased susceptibility to cell death is noted in the proband and in the carrier mother fibroblasts (Figure 2F). Within the trio, we observed that the proband's proliferation was significantly reduced compared to the father's cells, yet significantly higher than the mother's (Figure 2G). Moreover, cell death was significantly higher in the carrier mother compared to both the proband and the carrier father (Figure 2H). Furthermore, patient-derived cells showed reduced proliferative capacity and increased levels of cell death compared to control cell lines (Additional Figure 1A and 1B).

***POLR3A* heterozygote mutations can impact lipid and transcriptional profiles**

Given the observed cellular phenotypes and the known role of RNA Polymerase III in metabolic homeostasis, we investigated whether *POLR3A* variants were associated with distinct alterations in lipid and gene expression profiles. We employed a trio-based design using each parent as a genetically matched control, enabling mutation-specific comparisons between the proband and each carrier parent. This allowed us to dissect the individual contribution of each variant to the observed transcriptomic and lipidomic alterations.

We first performed untargeted lipidomic analysis in primary fibroblasts from the heterozygous parents (CARRIER MOTHER and CARRIER FATHER), from the proband (HLD7) and from her age- and sex- matched control (CTR HLD7). Principal Component Analysis (PCA) of differentially abundant lipids revealed a clear separation between control and variant-carrying samples, with the proband positioned half-in-between the parents, suggesting a combined effect of the two mutations (Figure 3A, left). Moreover, specific sets of lipids had a dysregulated abundance, particularly diacylglycerolipids and plasma membrane components (Figure 3A, right). Specifically, when comparing the affected patient (HLD7) vs a healthy control matched for age and sex (CTR HLD7),

30 lipids presented a differential abundance, with 22 being reduced and 8 being more present in HLD7 (Additional file 2). These lipids belonged to 11 different ontologies, the most abundant of which is represented by Phosphatidylserine (PS, Figure 3B). Furthermore, HLD7 presents 103 different species compared to the CARRIER MOTHER, all less abundant in the patient, and grouped in 18 ontologies of which Ether-linked phosphatidylethanolamine is the most represented (Additional file 2, Figure 3C). Lastly, when comparing HLD7 to the CARRIER FATHER, only 15 lipids belonging to 6 different ontologies are differentially abundant, 11 of which are less present in HLD7 (Additional file 2, Figure 3D). Interestingly, 2 lipids are found to be differentially abundant in all comparisons made, and these are PS 36:4 and PS 34:1|PS 18:0_16:1 (Figure 3E). To link the mutations in the RNA Polymerase III complex with the observed lipidomic dysfunctions, we sought to verify whether a transcriptional dysfunction could be a player between the phenomena. Indeed, we found that in term of transcriptional profiles the trio subjects tend to group separately from each other (Figure 3F), and we identified a high number of differentially expressed genes, (DEGs) 287 of which in common for all the conditions analyzed (Figure 3G). Interestingly, in the HLD7 vs CTR HLD7 condition, the one with the highest deregulation, 1394 genes are down-regulated, suggesting broad transcriptional repression (Additional file 3).

3.4 Compound heterozygous *POLR3A* variants are associated with a dysregulation in lipid abundance and alterations in lipid-related transcriptional programs

To further explore the mechanistic impact of compound heterozygous *POLR3A* variants, we performed integrative pathway enrichment analyses of the lipidomic and transcriptomic datasets. As mentioned, in the lipidomic profile HLD7 versus CTR HLD7 we obtained 30 differentially abundant lipids, with 22 reduced and 8 increased in the proband (Additional file 2). Through the BIOPAN webtool[23] we identified a dysregulation of several lipid metabolic pathways. Notably, the conversion of fatty acids (FA) (18:0) to FA (18:1) was significantly activated (Figure 4A), whilst conversions from FA (20:4) to FA (20:5), from FA (18:2) to FA (18:1) and from PC (42:1) to PS

(42:1) were significantly suppressed (Figure 4B). These lipid conversions are enzymatically mediated, and amongst these enzymes there is Phosphatidylserine synthase 1 (PTDSS1) which catalyzes the formation of phosphatidylserine from phosphatidylcholine. We thus wanted to investigate whether an alteration in its expression could explain the altered conversion but no significant transcriptional changes were highlighted, suggesting a possible post-transcriptional or metabolic regulation (Figure 4C).

Next, we examined transcriptomic alteration in HLD7 vs CTR HLD7. A total of 1925 transcripts were differentially expressed, of which 1394 are down-regulated whilst the remaining 531 are up-regulated (Additional file 3). Pathway enrichment analysis using WikiPathways (Figure 4D) and KEGG (Figure 4E), revealed an enrichment in lipid metabolism-related pathways, such as adipogenesis, familial partial lipodystrophy, white fat cell differentiation and differentiation of white and brown adipocyte, and regulation of lipolysis in adipocytes. These findings suggest that the lipidomic abnormalities observed in the proband are, at least in part, driven by altered expression of genes regulating lipid storage and remodeling.

To integrate lipidomic and transcriptomic signatures we used the MetaboAnalyst 5.0 webtool, highlighting several significantly impacted metabolic pathways. Amongst them, Glycerolipid Metabolism and Lysine degradation emerged as the most dysregulated, characterized by an accumulation of specific lipid species and concurrent downregulation of genes involved in their catabolism (Figure 4F).

3.5 The p.Gly1358Arg mutation primarily disrupts Lipid Homeostasis with limited impact on global gene expression.

To dissect the individual contribution of each POLR3A variant to the observed molecular phenotypes, we probed the trio approach which allows to dissect the contribution of each specific mutations, using each parent as a genetically matched control. We thus first compared the proband (HLD7) with the CARRIER MOTHER, as both share the p.Phe601Tyr mutation while only the

proband carries the p.Gly1358Arg one. This comparison enables the isolation of effects attributable to the p.Gly1358Arg mutation.

At the lipidomic level, this comparison yielded the highest number of differentially abundant lipid species across all trio comparisons, with 103 dysregulated lipids (Additional file 2). In contrast, only 896 genes were differentially expressed, representing the lowest transcriptomic divergence amongst all the analyzed comparisons (Additional file 3). These findings suggest that the p.Gly1358Arg mutation exerts a more pronounced effect on lipid metabolism rather than on the transcriptome.

Enzymatic pathway inference using BIOPAN revealed significant alterations in fatty acid conversion reactions. Specifically FA (18:0) to FA (18:1) and FA (20:5) to FA (20:4) conversions resulted significantly activated (Figure 5A), whilst the conversions from FA (20:5) to FA (22:5), FA (20:4) to FA (22:4) and FA (26:0) to FA (28:0) resulted suppressed (Figure 5B). Amongst the enzyme responsible for these processes there is stearoyl-Coenzyme A desaturase 1 (SCD1), involved in the synthesis of oleic acid (implicated in FA (18:1) FA (18:0), and the mRNA codifying for this enzyme results down-regulated in the pediatric patient (Figure 5C).

Transcriptomic pathway enrichment analysis revealed limited enrichment for lipid-related gene expression programs and only PPAR signaling was directly relevant to lipid biology (Figure 5D-5E). Indeed, most pathways were related to signaling cascades (e.g., PI3K-Akt, IL24, Wnt), cell cycle regulation, differentiation pathways and DNA processes (Figure 5D). Similarly, KEGG pathway analysis highlighted PI3K-Akt, Wnt, TGF-beta and PPAR signaling as top dysregulated pathways (Figure 5E), again suggesting that transcriptional changes driven by p.Gly1358Arg primarily affect general cellular processes rather than lipid-specific programs

Also in this case, we performed a MetaboAnalyst 5.0 analysis, highlighting Pyruvate metabolism and Glycerolipid Metabolism as the two top dysregulated metabolic pathways (Figure 5F).

3.6 The p.Phe601Tyr variant primarily affects transcriptional processes with minimal impact on lipid abundance

To elucidate the functional impact of the p.Phe601Tyr variant independently of p.Gly1358Arg, we compared HLD7 to her CARRIER FATHER, as both individuals carry the p.Gly1358Arg mutation, but only the proband harbors the additional p.Phe601Tyr variant. This approach allowed us to isolate the molecular consequences specifically attributable to p.Phe601Tyr. Strikingly, this comparison revealed the lowest number of differentially abundant lipids across all trio analysis, as only 15 lipid species were altered (Additional file 2). In contrast, the transcriptome profile exhibited substantial divergence, with 1722 DEGs (Additional file 3). These findings suggest that p.Phe601Tyr has a more profound impact on transcriptional regulation than on lipid abundance, in contrast to p.Gly1358Arg, which predominantly affects the lipidome. In this case, the conversion from FA (20:5) to FA (22:5) resulted significantly activated (Figure 6A), whilst the conversions from FA (18:0) to FA (20:0) and from FA (20:3) to FA (20:5) – via FA (20:4) were suppressed (Figure 6B). Additionally, a consistent suppression of the PC (42:1) to PS (42:1) was observed, mirroring the pattern seen in HLD7 vs CTR HLD7. Indeed, in this case, PTDSS1, catalyzer of this reaction, had an up-regulated trend, along with ELOVL5, a member of the ELO family (Figure 6C). Pathway enrichment analysis revealed some differences in lipid-related pathways, although to a lesser extent than in the comparison between HLD7 vs CTR HLD7 (Figure 5D-5E). Indeed, in this case WikiPathways analysis revealed alterations in Adipogenesis, white fat cell differentiation, differentiation of white and brown adipocytes, and transcriptional cascade regulating adipogenesis (Figure 6D). KEGG analysis further revealed dysregulation of glycosphingolipid biosynthesis, alongside pathways related to cell cycle progression and proliferation (Figure 6D-6E).

Finally, integrated lipidomic and transcriptomic analysis using MetaboAnalyst 5.0 analysis highlighted fructose and mannose metabolism and lysine degradation as the two top dysregulated integrated metabolic pathways (Figure 6F). These findings suggest that p.Phe601Tyr contributes to a distinct transcriptional remodeling, particularly in pathways linked to lipid biosynthesis and cellular metabolism, despite having limited impact on steady-state lipid abundance.

3.7 Oleic acid supplementation restores lipid droplet content and partially rescues proliferation deficits in proband fibroblasts.

To further explore the functional consequences of lipid imbalance in cells harboring *POLR3A* variants, we assessed lipid droplet accumulation in primary fibroblasts using Oil-Red O (ORO) staining. As expected, pediatric control fibroblasts exhibited a higher base-line level of ORO-positive lipid droplets compared to adult controls, consistent with the elevated lipid demand required for cellular growth and homeostasis during early development (Additional Figure 2). Notably, only the proband's cells exhibited a marked reduction in ORO-positive lipid droplets, compared to age- and sex- matched pediatric control (Figure 7A). Within the trio, lipid droplets quantification revealed that father's cells, with the p.Gly1358Arg variant, had a significantly higher number of ORO-positive lipid droplets per cell compared to both mother's (p.Phe601Tyr) and HLD7 (p.Gly1358Arg/Phe601Tyr) cells, which showed similar lipid content (Figure 7B). Notably, HLD7 cells consistently exhibited a reduced number of lipid droplets relative to control cells, regardless of age, indicating that lipid droplets depletion represents a robust feature of the patient-derived cells (Additional Figure 2A).

To determine whether lipid droplet restoration could modulate cellular proliferation, we supplemented cultured cells with oleic acid (OA). a known inducer of lipid droplet biogenesis - for 48 hours. OA significantly increased lipid droplet content in HLD7, CTR HLD7, CARRIER FATHER and CTR FATHER, whilst mothers' cells did not show any increase in lipid droplet content (Figure 7C, D). We observed a marked increase in lipid droplet accumulation in the proband's cells — approximately sixfold compared to untreated cells — a response not seen in the other cell lines (in which the increase was of maximum 1.5 fold) (Figure 7D). Despite this strong induction, HLD7 fibroblasts maintained a lower absolute lipid droplet content compared to the father's cells and remained similar to the mother's (Figure 7E).

We next assessed whether OA-induced lipid restoration impacted cellular proliferation. Notably, OA treatment ameliorated proliferation deficits across all trio members, narrowing differences between

parents while retaining the distinct proliferative impairment in the proband (Figure 7F, Figure 7G). No significant changes in cell death were observed across trio samples following OA supplementation (Figure 7H and Additional Figure 2B).

4. Discussion

RNA Polymerase III (Pol III)-related hypomyelinating leukodystrophies (POLR3-HLDs) are a group of rare genetic disorders caused by pathogenic variants in genes encoding subunits of Pol III. These disorders manifest with progressive neurological deterioration, hypomyelination, and motor dysfunction. While recent efforts have cataloged genotype–phenotype correlations based on large-scale clinical data and international registries(46), the cellular and molecular mechanisms linking *POLR3A* mutations to the disease phenotype remain poorly understood. Clarifying these pathways is essential for developing targeted therapeutic strategies(18).

In this study we provide novel molecular evidence on the intricate relationship between genetic mutations in *POLR3A* and the resulting hypomyelinating leukodystrophy employing a comprehensive approach combining the evaluation of cellular behavior with lipidomic and transcriptomic analyses. We exploit fibroblast cell lines from a family trio composed of a pediatric patient harboring compound heterozygous *POLR3A* variants (p.Phe601Tyr and p.Gly1358Arg), and her heterozygous carrier parents. Our multi-omics profiling reveals that each mutation exerts distinct and non-redundant effects on cellular homeostasis, and their combined presence in the proband leads to a more severe phenotype characterized by impaired lipid metabolism, altered gene expression, and proliferative deficits. Interestingly recent studies also highlighted that mutations in POLR3A can lead to significant transcriptional dysfunctions in numerous experimental models (46). The proband's fibroblasts do not show significant reduction in POLR3A protein expression compared to healthy donor cells. Different studies performed both in primary fibroblast or in immortalized cellular experimental model (i.e. HEK239 and MO3.13) report effects of POLR3A mutations on protein expression on reduction of protein expression(6,48). In addition, it has been

reported that in patient fibroblasts carrying a compound heterozygous mutation in POLR3A c.3721G>A (p.Val1241Met) and the splicing region c.1771-6C>G the expression levels of Pol III target genes decrease (49). However, the overexpression of wt POLR3A protein rescued the normal expression levels whereas the overexpression of pVal1241Met mutation did not (49). Even though it was recently reported that overexpression of both wild-type and p.Cys767Phe POL3A in HeLa cells showed the opposite (50), our evidence—despite no changes in protein expression—supports, through bioinformatic analyses, the hypothesis that the mutated POLR3A is functionally impaired when compared to the wild-type.

Functionally, the proband's fibroblasts exhibited a reduced proliferation and an increased in cell death, compared to an age- and sex- matched control. Heterozygous carriers present distinguished behavior, suggesting that each mutation could contribute to a specific pathway which, when combined, caused the pathogenic phenotype. Importantly, despite molecular and cellular alterations observed in fibroblasts from the heterozygous carrier parents, both individuals are clinically healthy and do not exhibit neurological or systemic features associated with POLR3-HLD. Notably, no hypomyelination-related symptoms have been reported in either parent. We then performed lipidomic and transcriptomic analyses on the family trio - affected pediatric patient with biallelic *POLR3A* mutations, carrier mother, carrier father - and a healthy control matched for age and sex with the pediatric patient to assess in more detail the insights of these differences and pinpoint the specific effects of each mutation. Our lipidomic analysis uncovered marked differences in lipid abundance across genotypes. Interestingly, the p.Gly1358Arg variant had a stronger impact on lipid species levels, while the p.Phe601Tyr variant exerted a broader effect on gene expression. The proband's fibroblasts reflected a compounded signature of both defects, with disrupted lipid metabolism and altered transcriptional networks. This genotype-specific divergence suggests that the two variants may converge on the same pathological outcome via independent cellular pathways —lipid imbalance and transcriptional dysregulation, respectively.

Enrichment analyses reveal alterations in lipid-related pathways, adipogenesis, and glycosphingolipid biosynthesis. The identification of key enzymes such as stearoyl-Coenzyme A desaturase 1 (SCD1) and phosphatidylserine synthase 1 (PTDSS1) provides molecular insights into the possible mechanisms underlying lipid metabolism dysregulation. These results prompted us to investigate lipid accumulation as both a consequence of compound heterozygous mutations and as potential cause of reduced proliferation. The first notable observation was the significant difference in lipid content between pediatric and adult cells from healthy donors, suggesting that pediatric cells rely on larger quantities of lipids to maintain homeostasis. The marked reduction of lipids in the proband indicates a disruption in normal cellular function. As expected, oleic acid supplementation increased the number of lipid droplets in all cells, except for female adult cells, where the increase was slight and non-significant. The ratio between the supplemented and not-supplemented cells indicates that the proband's cells rely more heavily on lipid utilization than both pediatric and adult controls. This likely reflects a compensatory response to lipid deficiency; however, the increase in lipid droplets remains insufficient, suggesting impaired metabolic efficiency. We thus evaluated the role of this supplementation on cell proliferation, finding that there was a significant improvement in proband's cell proliferation suggesting that lipid droplets are fundamental for the correct cell behavior.

Taken together, our results support a model in which compound heterozygous mutations in *POLR3A* disrupt both lipid homeostasis and transcriptional networks, and that these effects are non-redundant and synergistic. While each heterozygous mutation is associated with specific transcriptional or metabolic alterations at the cellular level, these changes appear insufficient, on their own, to cause a disease phenotype. In contrast, the combined presence of both mutations, as observed in the proband, likely exceeds a pathological threshold, leading to synergistic cellular dysfunction and clinical manifestation. These findings advance our understanding of the genotype–phenotype continuum in POLR3-HLDs and point to lipid metabolism as a key pathogenic axis. Of course, we acknowledge limitations of this study. The use of fibroblasts as a proxy for CNS tissue

restricts direct conclusions about oligodendrocyte-specific defects. Moreover, the trio-based design —while powerful in controlling shared genetic background—does not control for age and sex, both of which could influence lipid profiles and gene expression. An additional limitation is that our findings derive from a single affected family, which necessarily constrains their generalizability. Future studies will therefore be essential to validate these results and similar transcriptional and metabolic dysfunctions in additional patients, should they be identified, either carrying the same POLR3A variants or distinct pathogenic mutations within POLR3A or related POLR genes. Thus, validation in larger, age- and sex-matched cohorts and in oligodendrocyte-lineage cells will be critical to generalize these findings. Even so, understanding the precise relationship between lipid metabolism and dysfunctional myelin growth is crucial for developing targeted interventions for individuals affected by POLR3-HLDs. Additionally, the study emphasizes the importance of personalized medicine, considering the distinct impact of different mutations on lipidomic and transcriptomic profiles.

5. Conclusions

In conclusion, this study provides the first integrative lipidomic and transcriptomic characterization of *POLR3A*-related hypomyelinating leukodystrophy in a family trio.

Our findings reveal distinct and complementary effects of the Phe601Tyr and Gly1358Arg mutations on cellular lipid homeostasis and transcriptional regulation. The partial rescue of proliferative deficits via oleic acid supplementation suggests further investigations in a wider cohort of patients, as this could potentially be a novel therapeutic window impacting on hypomyelinating leukodystrophy. Together, this work underscores the relevance of lipid metabolism in POLR3-HLD pathogenesis and lays the groundwork for future translational studies aimed at modulating metabolic pathways in leukodystrophy.

List of abbreviations

CNS: central nervous system

DEGs: differentially expressed genes

FA: fatty acids

FBS: fetal bovine serum

HLD: hypomyelinating leukodystrophies

LD: lipid droplets

OA: oleic acid

ORO: oil red O

PC: phosphatidylcholine

POLR3-HLDs: RNA Polymerase III (Pol III)-related HLDs

PS: phosphatidylserine

PTDSS1: phosphatidylserine synthase 1

R.E.U.: Rosetta Energy Unit

SCD1: stearoyl-Coenzyme A desaturase 1

Ethics approval and Consent to Partecipate: Ethics Committee of the Institute "Casa Sollievo Della Sofferenza" was collected (Casa Sollievo della Sofferenza Ethical Committee, approval number: 136/CE).

Availability of data and materials: The datasets generated and/or analysed during the current study are available in the GEO repository, GSEXXX.

Competing interests: The authors declare that they have no competing interests

Funding: Not applicable.

Authors' contributions: Conceptualization F.R; J.R. S.C.; Formal analysis F.R., A.C.; investigation F.R., A.C., S.C.D., L.E., A.A.S., M.H., I.F., M.M., F.N., D.T.; writing-original draft preparation F.R., A.C., S.C.D., J.R., S.C.; writing-review and editing, L.M., C.B., M.B., F.B., Y.V., E.B., F.N., D.T., D.R.; supervision, G.Z., A.L.V., D.R., J.R., S.C., C.C. All authors have read and approved the final manuscript.

Acknowledgments

The authors would like to thank the families who donated their cells in the belief that their contribution would further the research. This work was in part supported by Fondazione Cariplo within the LAMPO DI GENE initiative to CC; by a grant from the Italian Ministry of Health, R25-5×1000 to JR; by a grant from Fondazione Prosolidar, 508-2021_IT to ALV and JR. The authors gratefully acknowledge Fondazione per l'Ospedale dei Bambini Buzzi ETS. SC is grateful to Pediatric Clinical Research Centre Fondazione "Romeo and Enrica Invernizzi" for its support. Lipidomic analyses were performed with the support of the Unitech OMICS facility at the University of Milan.

Notes

F.R.: Present address: IFOM ETS – The AIRC Institute of Molecular Oncology, via Adamello 16, 20139 Milan, Italy

A.A.S: Present address: Agenzia Spaziale Italiana, Via del Politecnico snc, 00133 Rome, Italy

References:

1. Kevelam S, Steenweg M, Srivastava S, Helman G, Naidu S, Schiffmann R, et al. Update on Leukodystrophies: A Historical Perspective and Adapted Definition. Neuropediatrics. 2016 Aug 26;47(06):349–54.

2. Schiffmann R, Van Der Knaap MS. Invited Article: An MRI-based approach to the diagnosis of white matter disorders. Neurology. 2009 Feb 24;72(8):750–9.

3. Van Der Knaap MS, Schiffmann R, Mochel F, Wolf NI. Diagnosis, prognosis, and treatment of leukodystrophies. The Lancet Neurology. 2019 Oct;18(10):962–72.

4. Wolf NI, Vanderver A, Van Spaendonk RML, Schiffmann R, Brais B, Bugiani M, et al. Clinical spectrum of 4H leukodystrophy caused by *POLR3A* and *POLR3B* mutations. Neurology. 2014 Nov 18;83(21):1898–905.

5. Macintosh J, Perrier S, Pinard M, Tran LT, Guerrero K, Prasad C, et al. Biallelic pathogenic variants in POLR3D alter tRNA transcription and cause a hypomyelinating leukodystrophy: A case report. Front Neurol. 2023 Oct 13;14:1254140.

6. Bernard G, Chouery E, Putorti ML, Tétreault M, Takanohashi A, Carosso G, et al. Mutations of POLR3A Encoding a Catalytic Subunit of RNA Polymerase Pol III Cause a Recessive

Hypomyelinating Leukodystrophy. The American Journal of Human Genetics. 2011 Sept;89(3):415–23.

7. Dorboz I, Dumay-Odelot H, Boussaid K, Bouyacoub Y, Barreau P, Samaan S, et al. Mutation in *POLR3K* causes hypomyelinating leukodystrophy and abnormal ribosomal RNA regulation. Neurol Genet [Internet]. 2018 Dec [cited 2025 July 17];4(6). Available from: https://www.neurology.org/doi/10.1212/NXG.0000000000000289

8. Tétreault M, Choquet K, Orcesi S, Tonduti D, Balottin U, Teichmann M, et al. Recessive Mutations in POLR3B, Encoding the Second Largest Subunit of Pol III, Cause a Rare Hypomyelinating Leukodystrophy. The American Journal of Human Genetics. 2011 Nov;89(5):652–5.

9. Thiffault I, Wolf NI, Forget D, Guerrero K, Tran LT, Choquet K, et al. Recessive mutations in POLR1C cause a leukodystrophy by impairing biogenesis of RNA polymerase III. Nat Commun [Internet]. 2015 July 7 [cited 2025 July 17];6(1). Available from: https://www.nature.com/articles/ncomms8623

10. Terhal PA, Vlaar JM, Middelkamp S, Nievelstein RAJ, Nikkels PGJ, Ross J, et al. Biallelic variants in POLR3GL cause endosteal hyperostosis and oligodontia. Eur J Hum Genet. 2020 Jan;28(1):31–9.

11. Dumay-Odelot H, Durrieu-Gaillard S, Da Silva D, Roeder RG, Teichmann M. Cell growth- and differentiation-dependent regulation of RNA polymerase III transcription. Cell Cycle. 2010 Sept 15;9(18):3711–23.

12. Lata E, Choquet K, Sagliocco F, Brais B, Bernard G, Teichmann M. RNA Polymerase III Subunit Mutations in Genetic Diseases. Front Mol Biosci [Internet]. 2021 July 30 [cited 2025 July 17];8. Available from: https://www.frontiersin.org/articles/10.3389/fmolb.2021.696438/full

13. Ramsay EP, Abascal-Palacios G, Daiß JL, King H, Gouge J, Pilsl M, et al. Structure of human RNA polymerase III. Nat Commun [Internet]. 2020 Dec 17 [cited 2025 July 17];11(1). Available from: https://www.nature.com/articles/s41467-020-20262-5

14. Fernández-Tornero C, Moreno-Morcillo M, Rashid UJ, Taylor NMI, Ruiz FM, Gruene T, et al. Crystal structure of the 14-subunit RNA polymerase I. Nature. 2013 Oct 31;502(7473):644–9.

15. Rey F, Esposito L, Maghraby E, Mauri A, Berardo C, Bonaventura E, et al. Role of epigenetics and alterations in RNA metabolism in leukodystrophies. Wiley Interdiscip Rev RNA. 2024;15(3):e1854.

16. Meschkat M, Steyer AM, Weil MT, Kusch K, Jahn O, Piepkorn L, et al. White matter integrity in mice requires continuous myelin synthesis at the inner tongue. Nat Commun [Internet]. 2022 Mar 4 [cited 2025 July 17];13(1). Available from: https://www.nature.com/articles/s41467-022-28720-y

17. Poitelon Y, Kopec AM, Belin S. Myelin Fat Facts: An Overview of Lipids and Fatty Acid Metabolism. Cells. 2020 Mar 27;9(4):812.

18. Nowacki JC, Fields AM, Fu MM. Emerging cellular themes in leukodystrophies. Front Cell Dev Biol [Internet]. 2022 Aug 8 [cited 2025 July 17];10. Available from: https://www.frontiersin.org/articles/10.3389/fcell.2022.902261/full

19. Aerts JM, Groener JE, Kuiper S, Donker-Koopman WE, Strijland A, Ottenhoff R, et al. Elevated globotriaosylsphingosine is a hallmark of Fabry disease. Proc Natl Acad Sci U S A. 2008 Feb 26;105(8):2812–7.

20. Maan K, Baghel R, Dhariwal S, Sharma A, Bakhshi R, Rana P. Metabolomics and transcriptomics based multi-omics integration reveals radiation-induced altered pathway networking and underlying mechanism. npj Syst Biol Appl. 2023 Sept 9;9(1):42.

21. Prasad MR, Engelman RM, Jones RM, Das DK. Effects of oxyradicals on oxymyoglobin. Deoxygenation, haem removal and iron release. Biochemical Journal. 1989 Nov 1;263(3):731–6.

22. Shooshtari P, Huang H, Cotsapas C. Integrative Genetic and Epigenetic Analysis Uncovers Regulatory Mechanisms of Autoimmune Disease. Am J Hum Genet. 2017 July 6;101(1):75–86.

23. Alvarado CX, Makarious MB, Weller CA, Vitale D, Koretsky MJ, Bandres-Ciga S, et al. omicSynth: An open multi-omic community resource for identifying druggable targets across neurodegenerative diseases. Am J Hum Genet. 2024 Jan 4;111(1):150–64.

24. Huang PS, Ban YEA, Richter F, Andre I, Vernon R, Schief WR, et al. RosettaRemodel: a generalized framework for flexible backbone protein design. PLoS One. 2011;6(8):e24109.

25. Stein A, Kortemme T. Improvements to robotics-inspired conformational sampling in rosetta. PLoS One. 2013;8(5):e63090.

26. Park H, Bradley P, Greisen P, Liu Y, Mulligan VK, Kim DE, et al. Simultaneous Optimization of Biomolecular Energy Functions on Features from Small Molecules and Macromolecules. J Chem Theory Comput. 2016 Dec 13;12(12):6201–12.

27. Frenz B, Lewis SM, King I, DiMaio F, Park H, Song Y. Prediction of Protein Mutational Free Energy: Benchmark and Sampling Improvements Increase Classification Accuracy. Front Bioeng Biotechnol. 2020;8:558247.

28. Guerois R, Nielsen JE, Serrano L. Predicting changes in the stability of proteins and protein complexes: a study of more than 1000 mutations. J Mol Biol. 2002 July 5;320(2):369–87.

29. Delgado J, Radusky LG, Cianferoni D, Serrano L. FoldX 5.0: working with RNA, small molecules and a new graphical interface. Bioinformatics. 2019 Oct 15;35(20):4168–9.

30. Rodrigues CHM, Pires DEV, Ascher DB. DynaMut2: Assessing changes in stability and flexibility upon single and multiple point missense mutations. Protein Sci. 2021 Jan;30(1):60–9.

31. Pejaver V, Urresti J, Lugo-Martinez J, Pagel KA, Lin GN, Nam HJ, et al. Inferring the molecular and phenotypic impact of amino acid variants with MutPred2. Nat Commun. 2020 Nov 20;11(1):5918.

32. Varadi M, Anyango S, Deshpande M, Nair S, Natassia C, Yordanova G, et al. AlphaFold Protein Structure Database: massively expanding the structural coverage of protein-sequence space with high-accuracy models. Nucleic Acids Res. 2022 Jan 7;50(D1):D439–44.

33. Cheng J, Novati G, Pan J, Bycroft C, Žemgulytė A, Applebaum T, et al. Accurate proteome-wide missense variant effect prediction with AlphaMissense. Science. 2023 Sept 22;381(6664):eadg7492.

34. Sim NL, Kumar P, Hu J, Henikoff S, Schneider G, Ng PC. SIFT web server: predicting effects of amino acid substitutions on proteins. Nucleic Acids Res. 2012 July;40(Web Server issue):W452-457.

35. Adzhubei IA, Schmidt S, Peshkin L, Ramensky VE, Gerasimova A, Bork P, et al. A method and server for predicting damaging missense mutations. Nat Methods. 2010 Apr;7(4):248–9.

36. Steinhaus R, Proft S, Schuelke M, Cooper DN, Schwarz JM, Seelow D. MutationTaster2021. Nucleic Acids Res. 2021 July 2;49(W1):W446–51.

37. Pir MS, Timucin E. AFFIPred: AlphaFold2 structure-based Functional Impact Prediction of missense variations. Protein Sci. 2025 Feb;34(2):e70030.

38. Yurtseven A, Keller S, Hirsch P, Kalinina OV, Gress A. StructMAn 2.0 Web: a web server for structural annotation of protein sequences and mutations. Nucleic Acids Res. 2025 July 7;53(W1):W528–33.

39. Katsonis P, Lichtarge O. Meta-EA: a gene-specific combination of available computational tools for predicting missense variant effects. Nat Commun. 2025 Jan 2;16(1):159.

40. Wu T, Hu E, Xu S, Chen M, Guo P, Dai Z, et al. clusterProfiler 4.0: A universal enrichment tool for interpreting omics data. The Innovation. 2021 Aug;2(3):100141.

41. Heberle H, Meirelles GV, Da Silva FR, Telles GP, Minghim R. InteractiVenn: a web-based tool for the analysis of sets through Venn diagrams. BMC Bioinformatics [Internet]. 2015 May 22 [cited 2025 July 17];16(1). Available from: https://bmcbioinformatics.biomedcentral.com/articles/10.1186/s12859-015-0611-3

42. Molenaar MR, Jeucken A, Wassenaar TA, van de Lest CHA, Brouwers JF, Helms JB. LION/web: a web-based ontology enrichment tool for lipidomic data analysis. Gigascience. 2019 June 1;8(6):giz061.

43. Gaud C, C Sousa B, Nguyen A, Fedorova M, Ni Z, O'Donnell VB, et al. BioPAN: a web-based tool to explore mammalian lipidome metabolic pathways on LIPID MAPS. F1000Res. 2021;10:4.

44. Pang Z, Zhou G, Ewald J, Chang L, Hacariz O, Basu N, et al. Using MetaboAnalyst 5.0 for LC-HRMS spectra processing, multi-omics integration and covariate adjustment of global metabolomics data. Nat Protoc. 2022 Aug;17(8):1735–61.

45. Pang Z, Chong J, Zhou G, de Lima Morais DA, Chang L, Barrette M, et al. MetaboAnalyst 5.0: narrowing the gap between raw spectra and functional insights. Nucleic Acids Res. 2021 July 2;49(W1):W388–96.

46. Michell-Robinson MA, Perrier S, Gauthier S, Derksen A, Sabbagh Q, Girbig M, et al. Comprehensive Genotype-Phenotype Analysis in POLR3-Related Disorders. HGG Adv. 2025 July 18;100481.

47. Ng PC, Henikoff S. SIFT: Predicting amino acid changes that affect protein function. Nucleic Acids Res. 2003 July 1;31(13):3812–4.

48. Choquet K, Forget D, Meloche E, Dicaire MJ, Bernard G, Vanderver A, et al. Leukodystrophy-associated POLR3A mutations down-regulate the RNA polymerase III transcript and important regulatory RNA BC200. Journal of Biological Chemistry. 2019 May;294(18):7445–59.

49. Zanette V, Reyes A, Johnson M, Do Valle D, Robinson AJ, Monteiro V, et al. Neurodevelopmental regression, severe generalized dystonia, and metabolic acidosis caused by *POLR3A* mutations. Neurol Genet [Internet]. 2020 Dec [cited 2025 July 22];6(6). Available from: https://www.neurology.org/doi/10.1212/NXG.0000000000000521

50. Ruan D dan, Ruan X lin, Wang R, Lin X fu, Zhang Y ping, Lin B, et al. Clinical phenotype and genetic function analysis of a family with hypomyelinating leukodystrophy-7 caused by POLR3A mutation. Sci Rep [Internet]. 2024 Apr 1 [cited 2025 July 22];14(1). Available from: https://www.nature.com/articles/s41598-024-58452-6

Figure legends

Figure 1. Inheritance, Localization, Structural Impact and Predicted Functional Consequences of two POLR3A variants. (A) Family Tree. (B) Sanger sequencing highlighting the presence of mutations in primary fibroblasts. (C) POLR3A gene structure and schematic view of the variations localization in human POLR3A protein sequence. (D) Disease-associated mutations (F601Y and G1358R) are mapped on a cartoon representation of human POLR3A protein together with their AM score (red spheres indicates the residue associated with each mutation). (E) Computed change in stability (ΔΔG), as predicted by Rosetta ΔΔG, FoldX, and DynaMut 2.0 (F) Intermolecular interactions that are acquired upon amino acid mutation (orange sticks) with respect to wild-type (wt) residue (highlighted in green sticks). For the sake of clarity, only acquired contacts are labelled. Dashed lines represent atomic interactions report in the legend. (G) Predicted alteration in molecular mechanism upon amino acid mutation, as predicted by MutPred2.

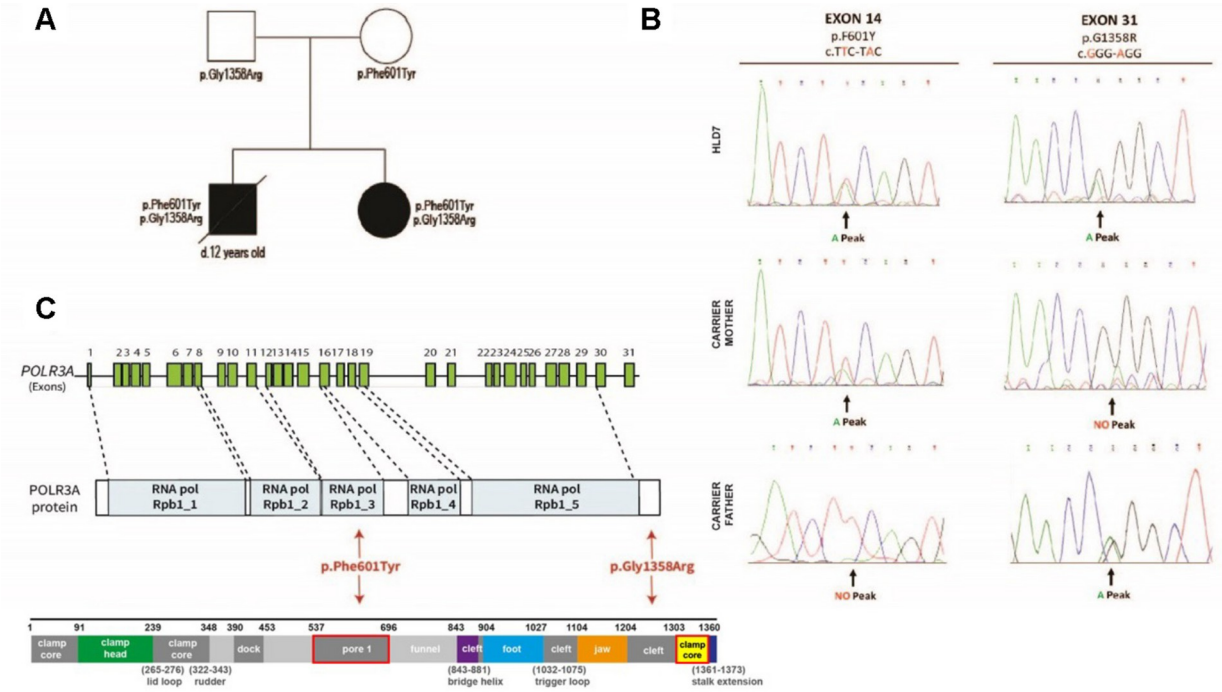

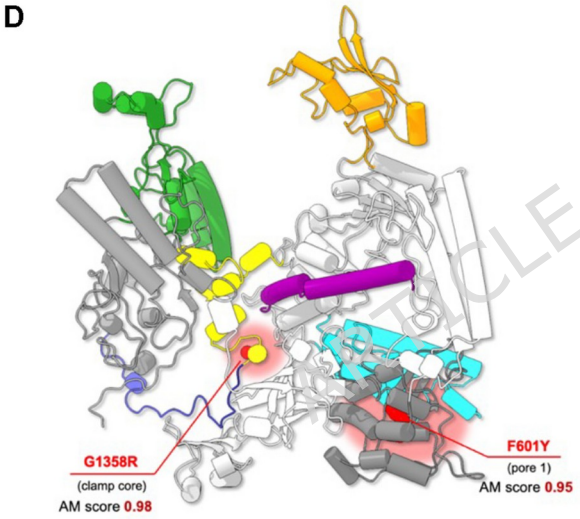

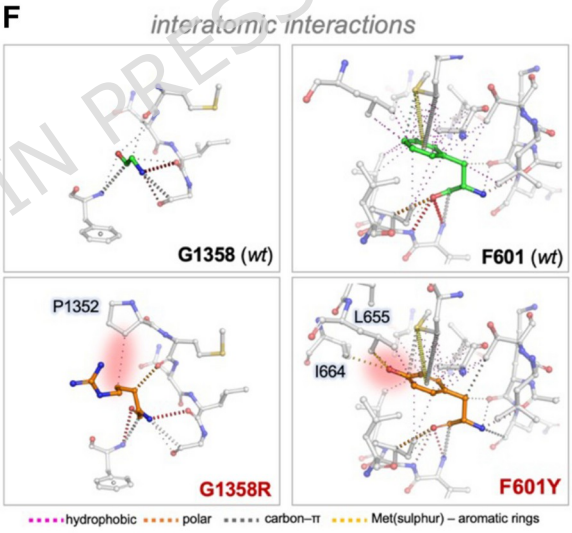

E

predicted change in stability (ΔΔG)

	F601Y	G1358R
Rosetta ΔΔG	**0.26** kcal/mol (0.89 R.E.U.)	**0.83** kcal/mol (2.80 R.E.U.)
FoldX	**1.39** kcal/mol (destabilizing)	**2.74** kcal/mol (destabilizing)
DynaMut 2.0	**0.34** kcal/mol (destabilizing)	**0.28** kcal/mol (destabilizing)

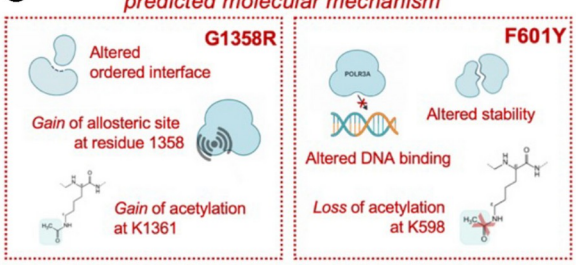

Figure 2. Features of isolated primary fibroblasts. A) POLR3A mRNA was quantified by qPCR in each family member versus sex- and age-matched controls B) qPCR was used to assess POLR3A mRNA expression within the trio, normalizing each heterozygous parent to the proband. C) Western Blot analysis showing the protein expression of POLR3A in each family member compared to sex and age-matched controls and D) normalizing heterozygous parent to the proband. E) Growth curves and F) % of death cells of each family fibroblast line compared to matched healthy samples measured every 7 days for a total of 21 days. G) Growth curves and H) % of dead cells among the family trio members. Data are expressed as mean ± SEM. All the Statistical analyses were performed on three independent experiments, using GraphPad Prism 8, through a One-Way or Two-Way ANOVA test followed by Sidak test for multiple comparisons, when required. * $p \leq 0.05$, ** $p \leq 0.01$, *** $p \leq 0.001$, **** $p \leq 0.0001$ amongst indicated comparisons.

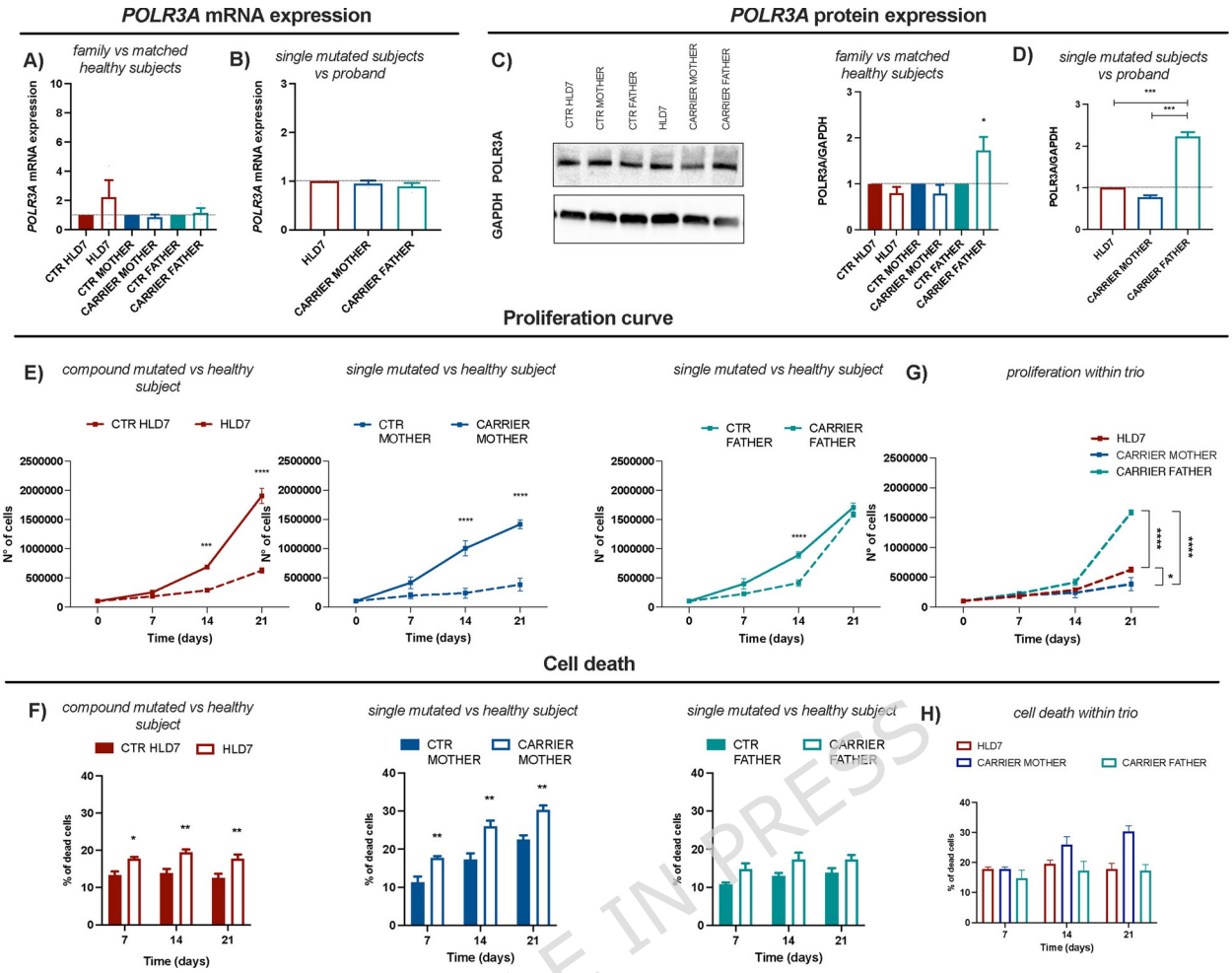

Figure 3. Lipidomic and transcriptomic analysis in a POLR3A-mutated family. (A): On the left, Principal Component Analysis (PCA) reporting the separation in lipidomic profiles of CTR HLD7, HLD7, CARRIER FATHER and CARRIER MOTHER, and on the right a heatmap as obtained with LION Enrichment webtool highlighting the grouping of different species dysfunction. Pie charts highlight % of the dysregulated lipid species in (B) HLD7 vs CTR HLD7, (C) CARRIER MOTHER vs HLD7, (D) CARRIER FATHER vs HLD7. Lipid Species are as follows. PS= Phosphatidylserine, PE= Phosphatidylethanolamine, PC = Phosphatidylcholine, EtherPE= Ether-linked phosphatidylethanolamine, EtherLPE= Ether-linked lysophosphatidylethanolamine, Cer_NS= Ceramide non-hydroxyfatty acid-sphingosine, CER_NDS= Ceramide non-hydroxyfatty acid-dihydrosphingosine, CE= Cholesteryl ester, CAR= Acylcarnitine, TG= Triacylglycerol. (E) InteractiVenn analysis showing shared lipids amongst comparisons – in orange HLD7 vs. CTR HLD7; in green HLD7 vs. CARRIER MOTHER and in blue HLD7 vs. CARRIER FATHER (F) PCA reporting the separation in transcriptional profiles of CTR HLD7, HLD7, CARRIER FATHER and CARRIER MOTHER. vs patients. (G) InteractiVenn analysis showing shared genes amongst comparisons – in orange HLD7 vs. CTR HLD7; in green HLD7 vs. CARRIER MOTHER and in blue HLD7 vs. CARRIER FATHER.

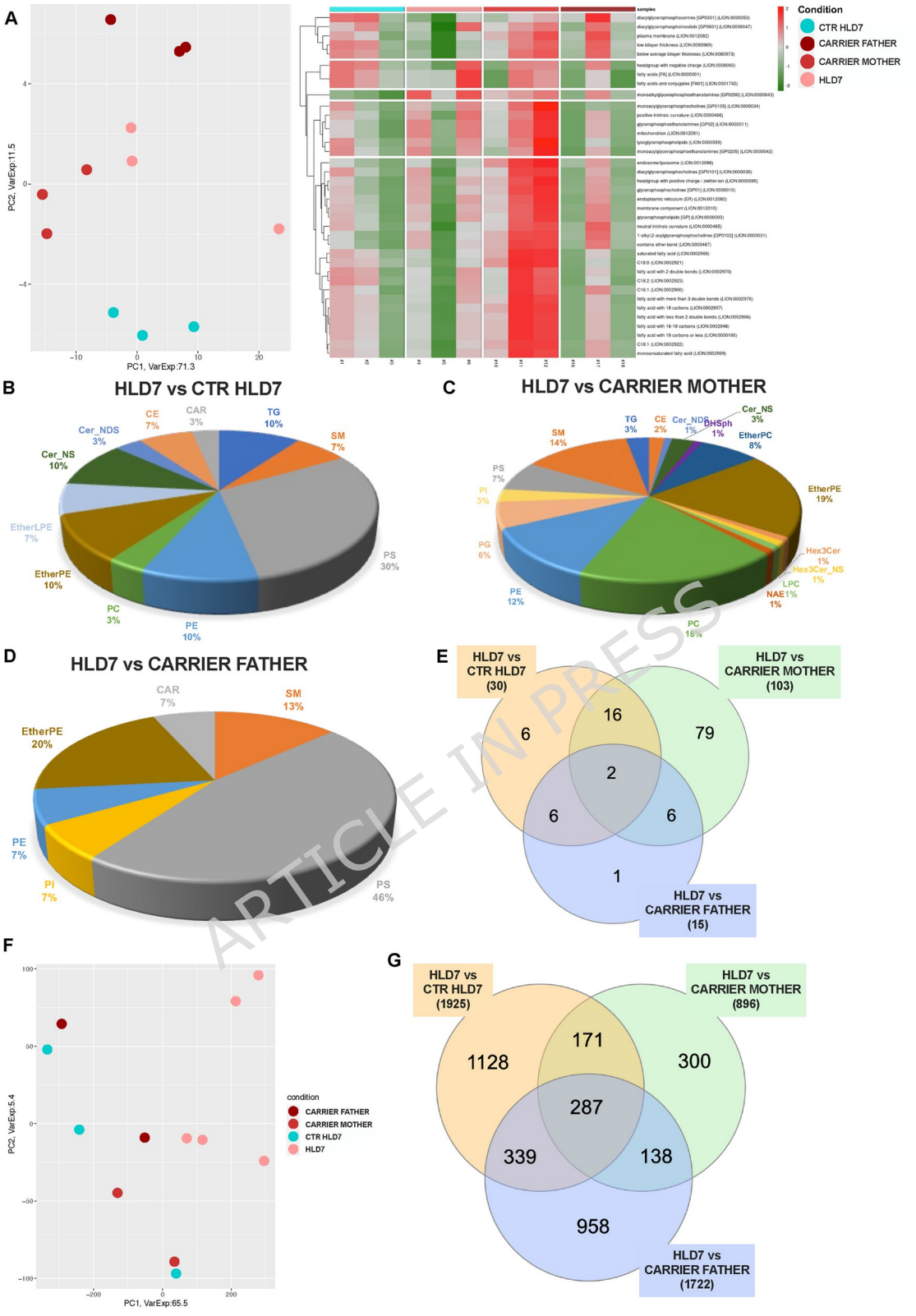

Figure 4: Lipidomic and transcriptomic profiles in patient fibroblasts harboring biallelic POLR3A mutations versus healthy control. BioPAN analysis for lipid and free fatty acids conversion shows active (A) and suppressed (B) pathways. (C) qPCR was performed to assess the expression of PTDSS1 in HLD7 vs CTR HLD7. Data are expressed as mean ± SEM of three independent experiments performed in triplicates (n=9). WikiPathways (D) and KEGG (E) enrichment analysis of differentially expressed targets following RNA-sequencing analyses. The dotplots report the top 20 most significant pathways, the y-axis represents the name of the pathway, the x-axis represents the rich factor, dot size represents the number of different genes involved. (F) MetaboAnalyst analysis shows integration of differentially expressed lipids and transcripts, highlighting a number of metabolic pathways involved plotted as bubble plot. The sizes of the bubbles are based on their x values, while the colors correspond to their y values. Glycerolipid Metabolism and Lysine degradation are the two most significant dysregulated pathways. Down-regulated targets are shown in green and up-regulated ones are shown in red; genes are shown as squares and lipids are shown as circles.

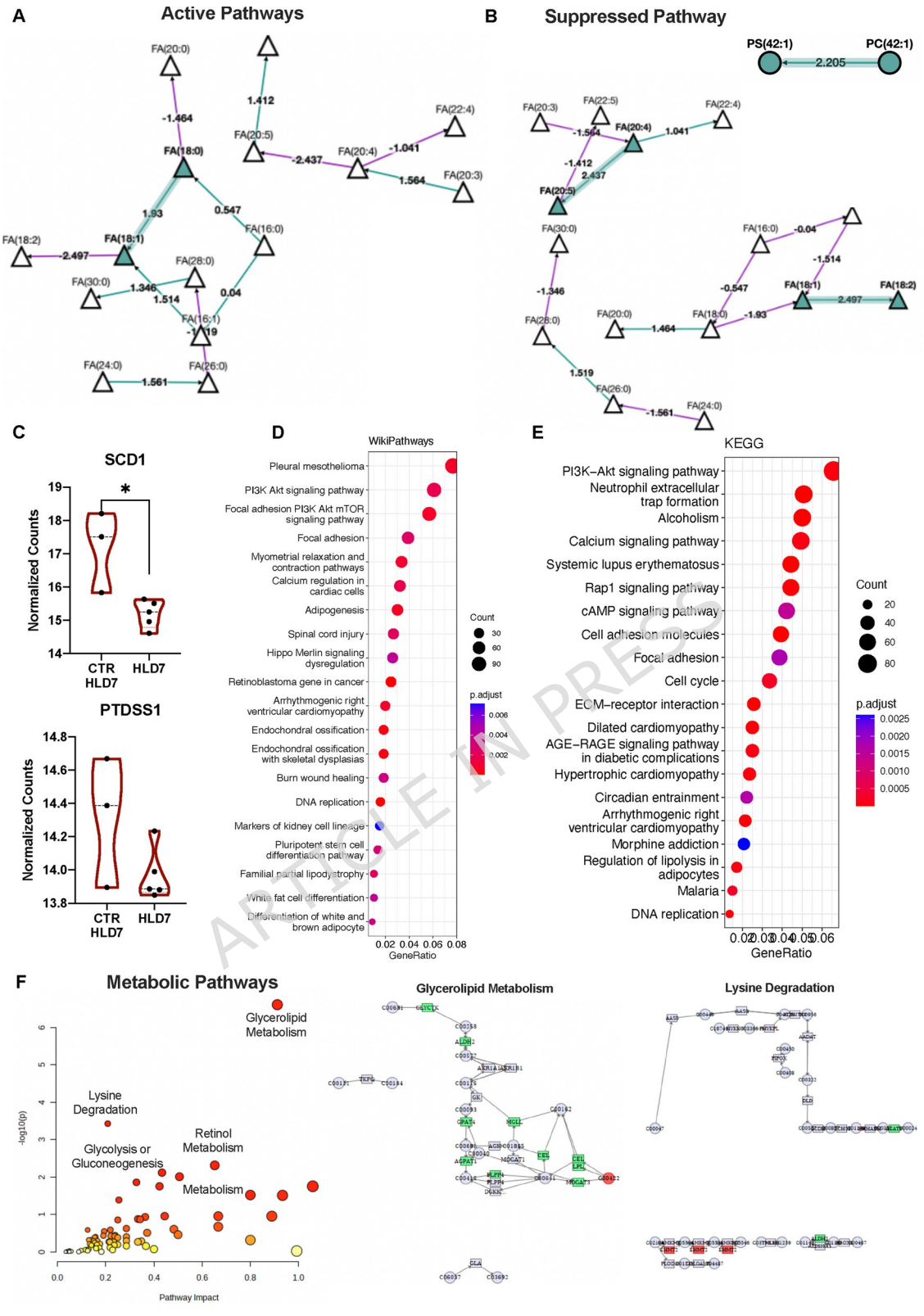

Figure 5: Lipidomic and transcriptomic profiles in a patient harboring biallelic POLR3A mutations versus carrier mother. BioPAN analysis for lipid and free fatty acids conversion shows active (A) and suppressed (B) pathways. (C) qPCR was performed to assess the expression of SCD1 in HLD7 vs CARRIER MOTHER. Data are expressed as mean ± SEM of three independent experiments performed in triplicates (n=9, *$p<0.05$, vs CARRIER MOTHER). WikiPathways (D) and KEGG (E) enrichment analysis of differentially expressed targets following RNA-sequencing analyses. The dotplots report the top 20 most significant pathways, the y-axis represents the name of the pathway, the x-axis represents the rich factor, dot size represents the number of different genes involved. (F) MetaboAnalyst analysis shows integration of differentially expressed lipids and transcripts, highlighting a number of metabolic pathways involved plotted as bubble plot. The sizes of the bubbles are based on their x values, while the colors correspond to their y values. Pyruvate Metabolism and Glycerolipid Metabolism are the two most significant dysregulated pathways. Down-regulated targets are shown in green and up-regulated ones are shown in red, genes are shown as squares and lipids are shown as circles.

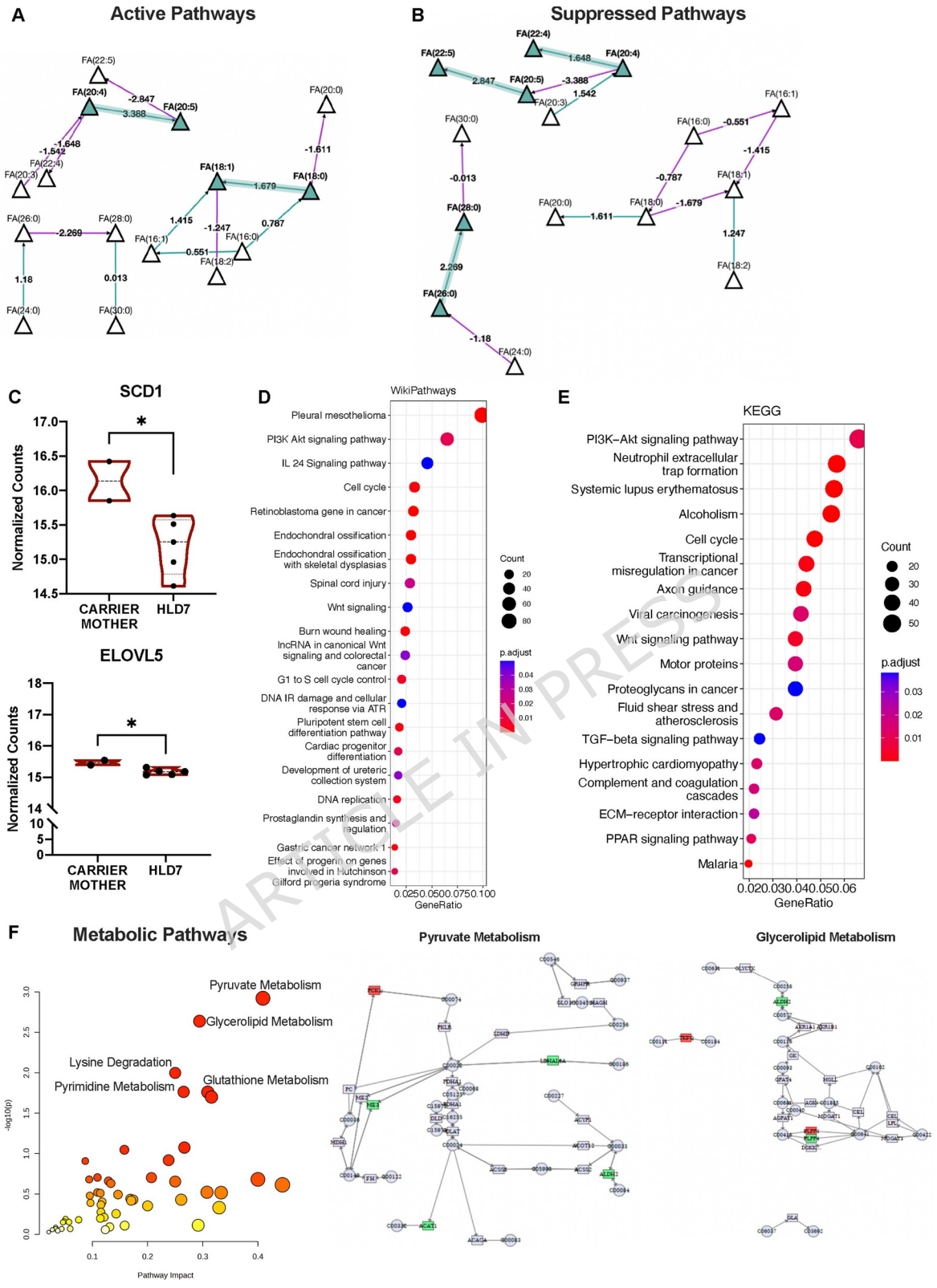

Figure 6: Lipidomic and transcriptomic profiles in a patient harboring biallelic POLR3A mutations versus carrier father. BioPAN analysis for lipid and free fatty acids conversion shows active (A) and suppressed (B) pathways. (C) qPCR was performed to assess the expression of PTDSS1 and ELOVL5 in HLD7 vs CARRIER FATHER. Data are expressed as mean ± SEM of three independent experiments performed in triplicates (n=9). WikiPathways (D) and KEGG (E) enrichment analysis of differentially expressed targets following RNA-sequencing analyses. The dotplots report the top 20 most significant pathways, the y-axis represents the name of the pathway, the x-axis represents the rich factor, dot size represents the number of different genes involved. (F) MetaboAnalyst analysis shows integration of differentially expressed lipids and transcripts, highlighting a number of metabolic pathways involved plotted as bubble plot. The sizes of the bubbles are based on their x values, while the colors correspond to their y values. Fructose and Mannose Metabolism and Lysine degradation are the two most significant dysregulated pathways. Down-regulated targets are shown in green and up-regulated ones are shown in red, genes are shown as squares and lipids are shown as circles.

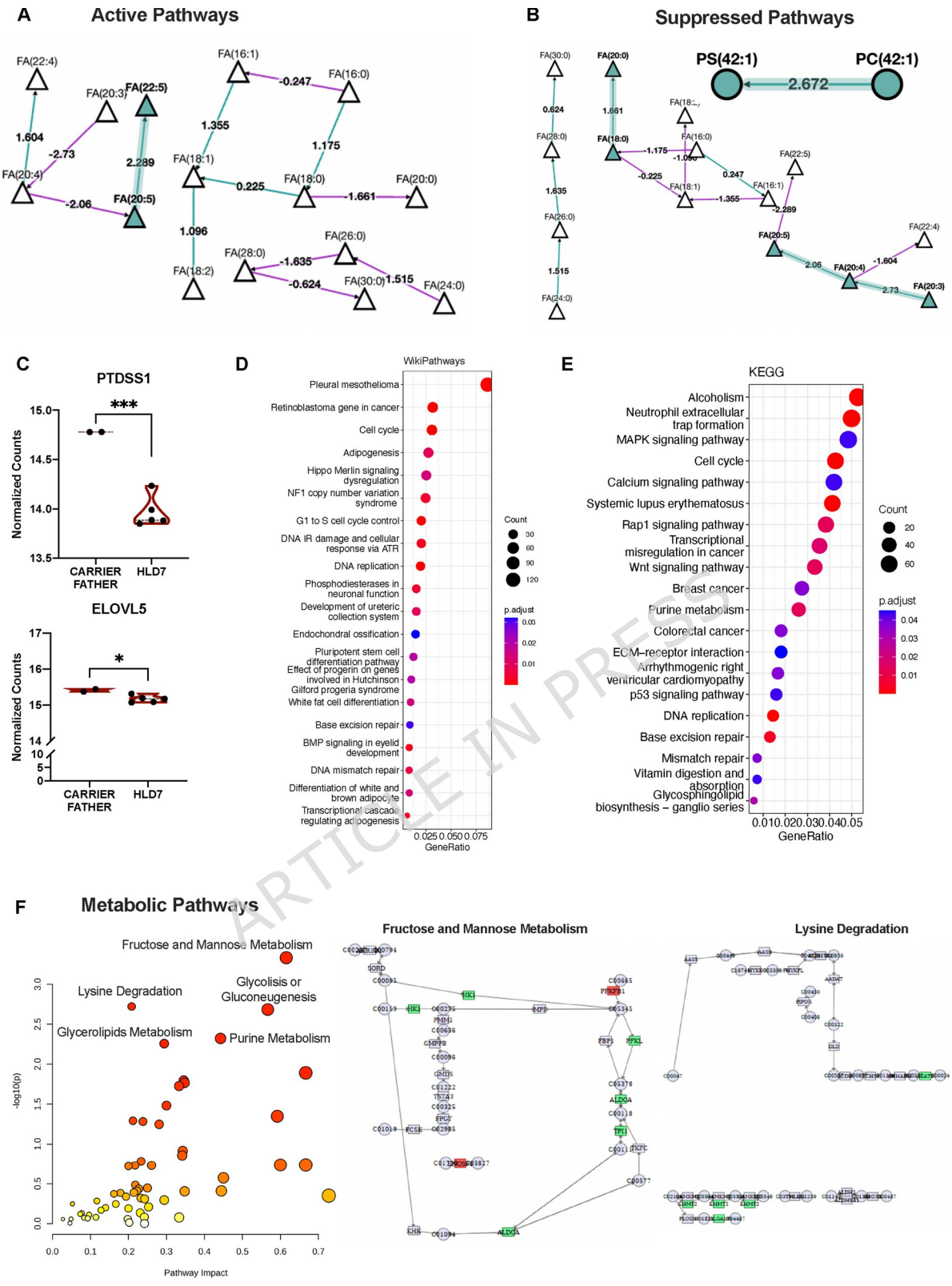

Figure 7. Oleic acid improved the lipid droplets accumulation. (A) Representative Oil Red O staining of lipid droplets in all fibroblast lines, with and without 50 µM Oleic Acid treatment. B) Lipid droplets quantification per cell across all cell lines for comparative analysis. C) Quantification of lipid droplets after 50 µM Oleic Acid treatment versus specific untreated cells. D) Increase of lipid droplets content in response to 50 µM Oleic Acid treatment expressed as ratio between treated and untreated cell (NT line). E) Number of lipid droplets per cell within the trio following 50 µM Oleic Acid treatment. F) Growth curves of family members versus sex- and age-matched controls after 50 µM Oleic Acid treatment. Cell count was expressed as ratio between treated and untreated cells (NT line). G) Growth kinetics and H) percentage of dead cells within the trio after 50 µM Oleic Acid exposure. Data are expressed as mean ± SEM. All the Statistical analyses were performed on three independent experiments, using GraphPad Prism 8, through a One-Way or Two-Way ANOVA test followed by Sidak test for multiple comparisons, when required. * $p \leq 0.05$, ** $p \leq 0.01$, *** $p \leq 0.001$, **** $p \leq 0.0001$ amongst indicated comparisons.

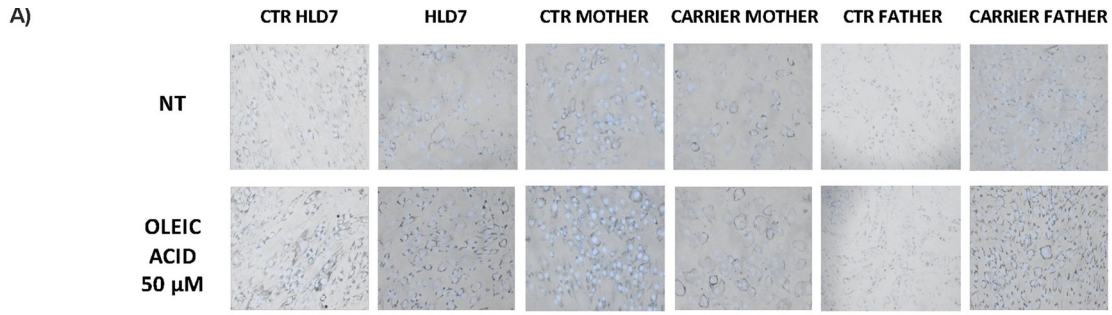

Lipid droplets quantification

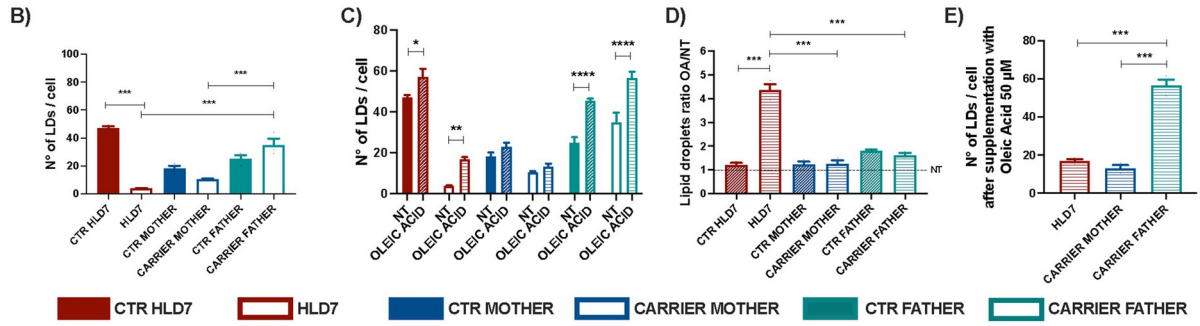

Proliferation curve

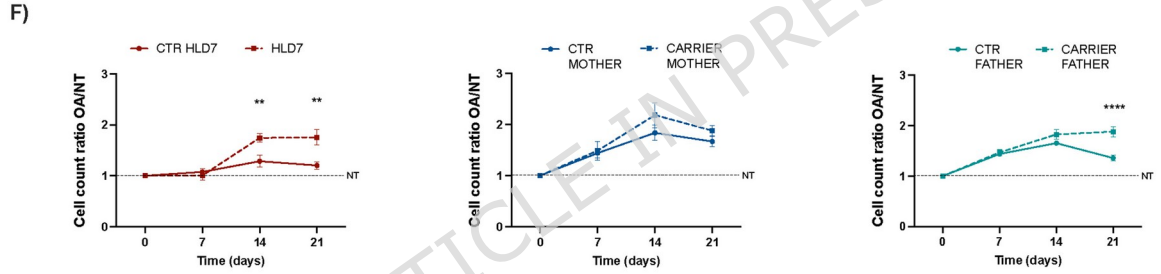

Effect of OA treatment within trio

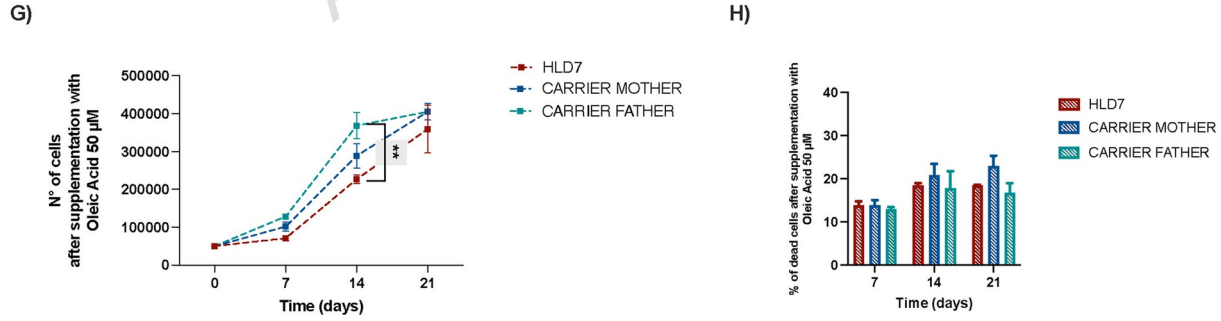

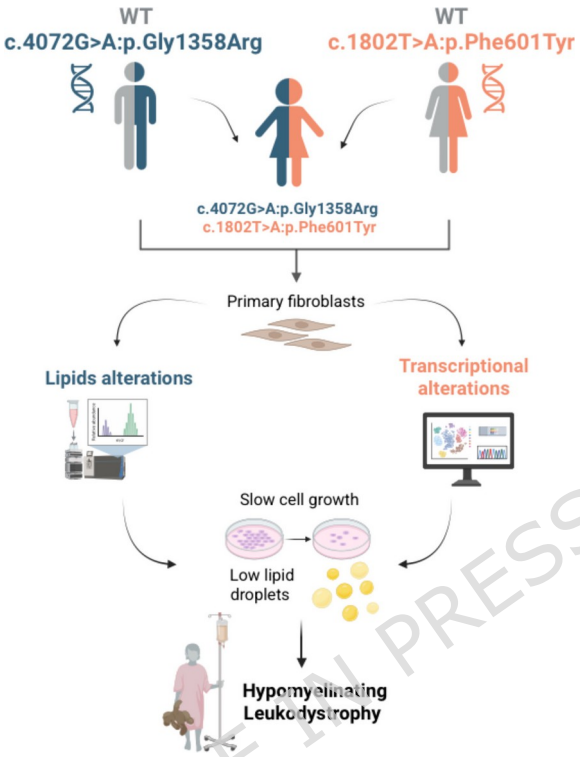

Additional Files

Additional Figure 1. Proliferation and cell death analyses performed in the proband (HLD7), heterozygous carrier parents, and additional non-familial healthy control fibroblast lines. **(A)** Growth curves showing the number of cells over time (0, 7, 14, and 21 days) for HLD7 fibroblasts compared with control fibroblasts matched for age and sex. **(B)** Quantification of cell death at the indicated time points. Despite variability among control samples, HLD7 fibroblasts consistently exhibit reduced proliferative capacity and increased cell death compared with all controls. Data are shown as mean ± SEM. Asterisks (*) indicate statistically significant differences between HLD7 and control cell lines at the same time point, as assessed by two-way ANOVA followed by Sidak's multiple comparisons test.

Additional Figure 2. Lipid droplet content and cell death analyses following oleic acid (OA) supplementation in proband (HLD7), heterozygous carrier parents, and additional non-familial healthy control fibroblast lines. **(A)** Quantification of lipid droplets per cell under basal conditions. **(B)** Cell death ratios following OA supplementation at the indicated time points. HLD7 fibroblasts display a markedly reduced number of lipid droplets compared with control fibroblasts, both at baseline and after OA supplementation, while OA treatment does not fully rescue the increased cell death observed in patient-derived cells. Data are shown as mean ± SEM.

Name and Extension: Additional_figure_1.pdf; Additional_figure_2.pdf.

Additional file 2: List of differentially abundant lipids. Name and Extension: additional_file_2.xls.

Additional file 3: List of differentially expressed genes. Name and Extension: additional_file_3.xls.